

# 1 Status of the Tibetan Plateau observatory (Tibet-Obs) and a 2 10-year (2009-2019) surface soil moisture dataset

3 Pei Zhang<sup>1,2</sup>, Donghai Zheng<sup>2</sup>, Rogier van der Velde<sup>1</sup>, Jun Wen<sup>3</sup>, Yijian Zeng<sup>1</sup>, Xin Wang<sup>4</sup>,  
4 Zuoliang Wang<sup>4</sup>, Jiali Chen<sup>2,5</sup>, Zhongbo Su<sup>1</sup>

5 <sup>1</sup>Faculty of Geo-Information Science and Earth Observation (ITC), University of Twente, Enschede,  
6 7514AE, the Netherlands

7 <sup>2</sup>National Tibetan Plateau Data Center, Key Laboratory of Tibetan Environmental Changes and Land Surface  
8 Processes, Institute of Tibetan Plateau Research, Chinese Academy of Sciences, Beijing, 100101, China

9 <sup>3</sup>College of Atmospheric Sciences, Chengdu University of Information Technology, Chengdu, 610225,  
10 China

11 <sup>4</sup>Northwest Institute of Eco-Environment and Resources, Chinese Academy of Sciences, Lanzhou, 730000,  
12 China

13 <sup>5</sup>College of Earth and Environmental Sciences, Lanzhou University, Lanzhou, 730000, China  
14

15 *Correspondence to:* Donghai Zheng ([zhengd@itpcas.ac.cn](mailto:zhengd@itpcas.ac.cn)), Z. (Bob) Su ([z.su@utwente.nl](mailto:z.su@utwente.nl))

16 **Abstract.** The Tibetan Plateau observatory of plateau scale soil moisture and soil temperature (Tibet-Obs)  
17 was established ten years ago, which has been widely used to calibrate/validate satellite- and model-based  
18 soil moisture (SM) products for their applications to the Tibetan Plateau (TP). This paper reports on the status  
19 of the Tibet-Obs and presents a 10-year (2009-2019) surface SM dataset produced based on *in situ*  
20 measurements taken at a depth of 5 cm collected from the Tibet-Obs that consists of three regional-scale SM  
21 monitoring networks, i.e. the Maqu, Naqu, and Ngari (including Ali and Shiquanhe) networks. This surface  
22 SM dataset includes the original 15-min *in situ* measurements collected by multiple SM monitoring sites of  
23 the three networks, and the spatially upscaled SM records produced for the Maqu and Shiquanhe networks.  
24 Comparisons between four spatial upscaling methods, i.e. arithmetic averaging, Voronoi diagram, time  
25 stability, and apparent thermal inertia, show that the arithmetic average of the monitoring sites with long-  
26 term (i.e.  $\geq$  six years) continuous measurements are found to be most suitable to produce the upscaled SM  
27 records. Trend analysis of the 10-year upscaled SM records indicates that the Shiquanhe network in the  
28 western part of the TP is getting wet while there is no significant trend found for the Maqu network in the  
29 east. To further demonstrate the uniqueness of the upscaled SM records in validating existing SM products  
30 for long term period (~10 years), the reliability of three reanalysis datasets are evaluated for the Maqu and  
31 Shiquanhe networks. It is found that current model-based SM products still show deficiencies in representing  
32 the measured SM dynamics in the Tibetan grassland (i.e. Maqu) and desert ecosystems (i.e. Shiquanhe). The  
33 dataset would also be valuable for calibrating/validating long-term satellite-based SM products, evaluation  
34 of SM upscaling methods, development of data fusion methods, and quantifying the coupling of SM and  
35 precipitation at 10-year scale. The dataset is available in the 4TU.ResearchData repository at  
36 <https://doi.org/10.4121/12763700.v7> (Zhang et al., 2020).

## 37 **1 Introduction**

38 The Tibetan Plateau observatory (Tibet-Obs) of plateau scale soil moisture and soil temperature (SMST) was  
39 setup in 2006 and became fully operational in 2010 with as objective of the calibration/validation of satellite-  
40 and model-based soil moisture (SM) products at regional scale (Su et al., 2011). The Tibet-Obs mainly  
41 consists of three regional-scale SMST monitoring networks, i.e. Maqu, Naqu, and Ngari, which cover  
42 different climate and land surface conditions across the Tibetan Plateau (TP) and each includes multiple *in*  
43 *situ* SMST monitoring sites. The SM data collected from the Tibet-Obs have been widely used in past decade  
44 to calibrate/validate satellite- and model-based SM products (e.g. Su et al., 2013; Zheng et al., 2015a;  
45 Colliander et al., 2017), and to evaluate and develop SM upscaling methods (e.g. Qin et al., 2013; 2015), to  
46 assess algorithms for the retrieval of SM for microwave remote sensing observations (e.g. van der Velde et  
47 al., 2014a; 2014b; Zheng et al., 2018a; 2018b; 2019) and fusion methods to merge *in situ* SM and satellite-  
48 or model-based products (e.g. Yang et al., 2020; Zeng et al., 2016).

49 Key information and outcomes of the main scientific applications using the Tibet-Obs SM data are  
50 summarized in Table 1. As shown in Table 1, the state-of-the-art satellite- and model-based products are  
51 useful but still show various types of deficiencies specific to the hydro-meteorological conditions on the TP,  
52 and further evaluation and improvement of these products remain imperative. In general, previous studies  
53 mainly focused on the evaluation of SM products using the Tibet-Obs data for short term period (i.e. less  
54 than five years), while up to now the Tibet-Obs has collected *in situ* measurements for more than 10 years.  
55 Development of a close to 10-year Tibet-Obs *in situ* SM dataset would further enhance the  
56 calibration/validation of long-term satellite- and model-based products, and is valuable for better  
57 understanding the hydro-meteorological response to climate change. However, SM is highly variable in both  
58 space and time, and data gaps in the availability of measurements taken from individual monitoring sites  
59 hinder scientific studies covering longer time periods, e.g. more than five years. Therefore, it is still  
60 challenging to obtain accurate long-term regional-scale SM due to the sparse nature of monitoring networks  
61 and highly variable soil conditions.

62 Spatial upscaling is usually necessary to obtain the regional-scale SM of an *in situ* network from multiple  
63 monitoring sites to match the footprint of satellite- or grid cell of model-based products. A frequently used  
64 approach for upscaling point-scale SM measurements to a spatial domain is the arithmetic average, mostly  
65 because of its simplicity (Su et al. 2011; 2013). Many other studies also adopted weighted averaging methods,  
66 whereby the weights are assigned to account for spatial heterogeneity in the area covered by *in situ*  
67 monitoring sites within the network. For instance, Colliander et al. (2017) employed Voronoi diagrams to  
68 determine the weights of individual monitoring sites within core regional-scale networks used for the  
69 worldwide validation of the Soil Moisture Active/Passive (SMAP) SM products. Dente et al. (2012a)  
70 established weights based on the topography and soil texture for the sites of the Tibet-Obs' Maqu network.  
71 Qin et al. (2013, 2015) derived the weights by minimizing a cost function between *in situ* SM of individual  
72 monitoring sites and a representative SM of the network that is estimated using the apparent-thermal-inertia-  
73 based (ATI) method (Gao et al., 2017). Alternative methods, such as time stability and ridge regression, have

74 been adopted in other investigations (i.e. Zhao et al., 2013, Kang et al., 2017). While a large number of studies  
75 have assessed the performance of different upscaling methods in other areas such as the Tonzi Ranch network  
76 in California and the Heihe watershed (Moghaddam et al., 2014, Wang et al., 2014), only a few investigations  
77 have been done for the TP (Gao et al., 2017, Qin et al., 2015). Since the number of monitoring sites changes  
78 over time due to damage of SM sensors in the Tibet-Obs, it is essential to evaluate and select an appropriate  
79 upscaling method for a limited number of monitoring sites (i.e.  $\leq$  four sites).

80 This paper reports on the status of the Tibet-Obs and presents a long-term *in situ* SM and spatially upscaled  
81 SM dataset for the period between 2009 and 2019. The 10-year SM dataset of Tibet-Obs includes the original  
82 15-min *in situ* measurements taken at a depth of 5 cm collected from the three regional-scale networks (i.e.  
83 Maqu, Naqu, and Ngari as shown in Fig. 1), and the continuous regional-scale SM produced using an  
84 appropriately selected spatial upscaling method. To achieve this, four methods are studied namely the  
85 arithmetic average (AA), Voronoi diagram (VD), time stability (TS), and apparent thermal inertia (ATI)  
86 methods. The seasonal dynamic and trend of the regional-scale SM time series are analysed and the 10-year  
87 SM dataset is used to validate three model-based SM products, e.g. ERA5-land (Muñoz-Sabater et al., 2018),  
88 MERRA2 (Modern-Era Retrospective Analysis for Research and Applications, version 2) (GMAO, 2015),  
89 and GLDAS Noah (Global Land Data Assimilation System with Noah Land Surface Model) (Rodell et al.,  
90 2004).

91 This paper is organized as follows. Section 2 describes the status of the Tibet-Obs and the *in situ* SM  
92 measurements, as well as the precipitation data and the three model-based SM products. Section 3 introduces  
93 the four SM spatial upscaling methods, Mann Kendall trend test and Sen's slope estimate, and performance  
94 metrics. Section 4 presents the inter-comparison of the four SM spatial upscaling methods, the production  
95 and analysis of regional-scale SM dataset for a 10-year period, and its application to validate the three model-  
96 based SM products. Section 5 provides the discussion and suggestions for maintaining Tibet-Obs. Section 6  
97 documents the information on data availability and the conclusions are drawn in Section 7.

## 98 **2 Data**

### 99 **2.1 Status of the Tibet-Obs**

100 The Tibet-Obs consists of the Maqu, Naqu, and Ngari (including Shiquanhe and Ali) regional-scale SMST  
101 monitoring networks (Fig. 1) that cover the cold humid climate, cold semiarid climate, and cold arid climate,  
102 respectively. Each network includes a number of monitoring sites that measure the SMST at different soil  
103 depths. Brief descriptions of each network and corresponding surface SM measurements taken at a depth of  
104 5 cm are given in following subsections. The readers are referred to the existing literature (Su et al., 2011;  
105 Dente et al. 2012a; Zhao et al., 2018) for additional information on the networks.

106 **2.1.1 Maqu network**

107 The Maqu network is located in the north-eastern edge of the TP (33°30'-34°15'N, 101°38'-102°45'E) at the  
108 first major bend of the Yellow River. The landscape is dominated by the short grass at elevations varying  
109 from 3400 to 3800 m. The climate type is characterized as cold-humid with cold dry winters and rainy  
110 summers. The mean annual air temperature is about 1.2 °C, with -10 °C for the coldest month (January) and  
111 11.7 °C for the warmest month (July) (Zheng et al., 2015a). The annual precipitation is about 600 mm that  
112 falls mainly in the warm season (May-October).

113 The Maqu network covers an area of approximately 40 km by 80 km and consists originally of 20 SMST  
114 monitoring sites installed in 2008 (Dente et al. 2012a). During the period between 2014 and 2016, eight new  
115 sites were installed due to the damage of several old monitoring sites by local people or animals. The basic  
116 information of each monitoring site is summarized in Table A1 (Su et al., 2011), and the typical  
117 characteristics of topography and land cover within the network are shown in Fig. 2 as well.

118 The Decagon 5TM ECH<sub>2</sub>O probes are used to measure the SMST at nominal depths of 5, 10, 20, 40, and 80  
119 cm (Fig. 3). The 5TM probe is a capacitance sensor measuring the dielectric permittivity of soil, and the Topp  
120 equation (Topp et al., 1980) is used to convert the dielectric permittivity to the volumetric SM. The accuracy  
121 of the 5TM volumetric SM was improved via a soil-specific calibration performed under laboratory  
122 conditions for each soil type found in the Maqu area (Dente et al. 2012a), leading to a decrease in the root  
123 mean square error (RMSE) from 0.06 to 0.02 m<sup>3</sup> m<sup>-3</sup> (Dente et al. 2012a). Table 2 provides the specific  
124 periods of data missing during each year and the total data lengths of surface SM for each monitoring site.  
125 Among these sites, the CST05, NST01, and NST03 have collected more than nine years of SM  
126 measurements, while the data records for the NST21, NST22, and NST31 are less than one year. In May  
127 2019, there were still 12 sites that provided SM data.

128 **2.1.2 Ngari network**

129 The Ngari network is located in the western part of the TP at the headwater of the Indus River. It consists of  
130 two SMST networks established around the cities of Ali and Shiquanhe, respectively. The landscape is  
131 dominated by a desert ecosystem at elevations varying from 4200 to 4700 m. The climate is characterized as  
132 cold-arid with a mean annual air temperature of 7.0 °C. The annual precipitation is less than 100 mm that  
133 falls mainly in the monsoon season (July-August) (van der Velde et al., 2014b).

134 The Shiquanhe network consisted originally of 16 SMST monitoring sites installed in 2010 (Su et al. 2011),  
135 and five new sites were installed in 2016. The basic information of each monitoring site is summarized in  
136 Table A3 (Su et al., 2011), and the typical characteristics of topography and land cover within the network  
137 are also shown in Fig. 4. The Decagon 5TM ECH<sub>2</sub>O probes were installed at depths of 5, 10, 20, 40, and  
138 60/80 cm to measure the SMST (Fig. 3). Table 3 provides the specific periods of data missing during each  
139 year and the total data lengths of surface SM for each site. Among these sites, the SQ02, SQ03, SQ06, and  
140 SQ14 have collected more than eight years of SM measurements, while the data records for the SQ13, SQ15,  
141 and SQ18 are less than two years. In August 2019, there were still 12 sites that provided SM data. The Ali

142 network comprises of four SM monitoring sites (Table A3), which will not be used for further analysis in  
143 this study due to limited number of monitoring sites and the availability of data records (Table 3).

### 144 **2.1.3 Naqu network**

145 The Naqu network is located in the Naqu river basin with an average elevation of 4500 m. The climate is  
146 characterized as cold semi-arid with cold dry winters and rainy summers. Over three-quarters of the total  
147 annual precipitation sum (400 mm) falls between June and August (Su et al., 2011). The landscape is  
148 dominated by short grass.

149 The network consists originally of five SMST monitoring sites installed in 2006 (Su et al. 2011), and six new  
150 sites were installed between 2010 and 2016. The basic information of each monitoring site is summarized in  
151 Table A5, and the typical topography and land cover within the network are shown in Fig. 5 as well. The  
152 Decagon 5TM ECH<sub>2</sub>O probes were installed at depths of 5/2.5, 10/7.5, 15, 30, and 60 cm to measure the  
153 SMST, and an on-site soil-specific calibration is reported in van der Velde (2010) and yielded a RMSE of  
154 0.029 m<sup>3</sup> m<sup>-3</sup>. Table 4 provides the specific periods of data missing during each year and the total data lengths  
155 of surface SM for each site. Among these sites, only two sites (Naqu and MS sites in Table A5) have collected  
156 SM measurements for more than six years, while the data records for the others are less than four years.  
157 Similar to the Ali network, the Naqu network will also not be used for the further analysis in this study due  
158 to limited number of monitoring sites and the availability of data records.

### 159 **2.2 Precipitation data**

160 Precipitation data is available from the dataset of daily climate data from Chinese surface meteorological  
161 stations. This dataset is maintained by the China Meteorological Administration (CMA) and based on the  
162 measurements from 756 basic and reference surface meteorological observation and automatic weather  
163 stations (AWS) in China from 1951 to present. The online dataset mainly includes seven meteorological  
164 variables such as air pressure, air temperature, relative humidity, wind speed, evaporation, sunshine duration,  
165 and precipitation. The precipitation data from two weather stations (see Fig. 1), i.e. Maqu (34°00'N,  
166 102°05'E) and Shiquanhe (32°30'N, 80°05'E) are used in this study. The available daily precipitation is the  
167 cumulative value for the period between 20h of previous day and 20h of current day at Beijing time, which  
168 is available from [https://data.cma.cn/data/detail/dataCode/SURF\\_CLI\\_CHN\\_MUL\\_DAY.html](https://data.cma.cn/data/detail/dataCode/SURF_CLI_CHN_MUL_DAY.html) (last access  
169 11 March 2021). The daily precipitation is summed up for each month to obtain the monthly cumulative  
170 value in this study, which can be found at <https://doi.org/10.4121/12763700.v7> (last access 16 April 2021).  
171 The monthly precipitation data for the period between 2009 and 2019 is mainly used in this study for the  
172 trend analysis (see Section 4.2).

## 173 **2.3 Model-based soil moisture products**

### 174 **2.3.1 ERA5-land soil moisture product**

175 ERA5-land is a reanalysis dataset produced by running land component of the ECMWF (European Centre  
176 for Medium-Range Weather Forecasts) ERA5 climate model (Albergel et al., 2018). ERA5-land provides  
177 SM data currently available from 1981 to present for every hour with a spatial resolution of 0.1°, and the data  
178 is available from <https://cds.climate.copernicus.eu/cdsapp#!/dataset/reanalysis-era5-land?tab> (last access 11  
179 March 2021). More information about the ERA5-land product readers are referred to Muñoz-Sabater et al.,  
180 (2018). The data of volumetric total soil water content for the top soil layer (0-7 cm) is used in this study.

### 181 **2.3.2 MERRA2 soil moisture product**

182 MERRA2 is an atmospheric reanalysis dataset produced by NASA using the Goddard Earth Observing  
183 System Model version 5 (GEOS-5) and atmospheric data assimilation system (ADAS), version 5.12.4.  
184 MERRA2 provides SM data currently available from 1980 to present at hourly time interval and spatial  
185 resolution of 0.5° (latitude) by 0.625° (longitude). The data is available from  
186 [https://disc.gsfc.nasa.gov/datasets/M2T1NXLND\\_5.12.4/summary](https://disc.gsfc.nasa.gov/datasets/M2T1NXLND_5.12.4/summary) (last access 11 March 2021). For more  
187 information about the MERRA2 product readers are referred to GMAO (2015). The liquid volumetric soil  
188 water content of the surface layer (0-5 cm) is used in this study.

### 189 **2.3.3 GLDAS Noah soil moisture product**

190 GLDAS-2.1 Noah is a combination of model-based and satellite observed meteorological data, such as  
191 Global Precipitation Climatology Project (GPCP) version 1.3, forced onto the Noah Model 3.6 in Land  
192 Information System (LIS) version 7 to simulate water and energy exchanges between land and atmosphere.  
193 GLDAS-2.1 Noah provides SM data currently available from 2000 to present at a 3-hourly time interval with  
194 a spatial resolution of 0.25°. The data is available from [https://disc.gsfc.nasa.gov/datasets/GLDAS  
195 \\_NOAH025\\_3H\\_2.1/summary](https://disc.gsfc.nasa.gov/datasets/GLDAS_NOAH025_3H_2.1/summary) (last access 11 March 2021). More details on the GLDAS Noah product can  
196 be found in Rodell et al. (2004). The liquid soil water content of the top soil layer (0-10 cm) is used in this  
197 study.

## 198 **3 Methods**

### 199 **3.1 Spatial upscaling of soil moisture measurements**

200 The principle of spatial upscaling a set of point measurements to an area is based on assigning weights to  
201 individual sites, often using additional information, in such way that the selected collection is representative  
202 for the selected domain. The method can in its simplest form be represented by a linear equation  
203 mathematically as follows:

$$204 \bar{\theta}_t^{ups} = \theta_t^{obs} \beta \quad (1a)$$

$$\boldsymbol{\theta}_t^{obs} = [\boldsymbol{\theta}_{t,1}^{obs}, \boldsymbol{\theta}_{t,2}^{obs}, \dots, \boldsymbol{\theta}_{t,N}^{obs}]^T \quad (1b)$$

where  $\bar{\boldsymbol{\theta}}_t^{ups}$  [ $\text{m}^3 \text{m}^{-3}$ ] represents the upscaled SM,  $\boldsymbol{\theta}_t^{obs}$  [ $\text{m}^3 \text{m}^{-3}$ ] represents the vector of SM measurements,  $N$  represents the total number of SM monitoring sites,  $t$  represents the time (e.g. the  $t^{\text{th}}$  day), and  $\beta$  [-] represents the vector with weights.

In this study, only the surface SM measurements taken from the Maqu and Shiquanhe networks are upscaled to obtain the regional-scale SM for 10-year (2009-2019) periods due to the availability of much longer records in comparison to the Naqu and Ali networks (see Section 2.1). Four upscaling methods are investigated and inter-compared with each other to find the most suitable method for the application to the Tibet-Obs. Brief descriptions of the selected upscaling methods are given in Appendix B. The arithmetic average (hereafter ‘‘AA’’) assigns an equal weight coefficient to each SM monitoring site (see Appendix B.1), and the Voronoi diagram (hereafter ‘‘VD’’) determines the weight based on the geographic distribution of all the SM monitoring sites (see Appendix B.2). The time stability method (hereafter ‘‘TS’’) regards the most stable site as representative site for the network (see Appendix B.3), and the apparent thermal inertia (ATI) method is based on the close relationship between apparent thermal inertia ( $\tau$ ) and SM (see Appendix B.4).

### 3.2 Trend analysis

The Mann-Kendall test and Sen’s slope estimate (Gilbert, 1987; Mann, 1945; Smith et al., 2012) are adopted to analyze the trend of the 10-year time series for the upscaled SM, model-based SM products (i.e. ERA5-land, GLDAS Noah, and MERRA2), and precipitation. Specifically, the trend analysis is based on the monthly data, and all the missing data is regarded as an equal value smaller than other valid data. The test consists of calculating the seasonal statistics  $S$  and its variance  $\text{VAR}(S)$  separately for each month during the 10-year period, and the seasonal statistics are then summed to obtain the  $Z$  metric.

For month  $i$  (e.g. January), the statistics  $S_i$  can be computed as:

$$S_i = \sum_{k=1}^9 \sum_{l=k+1}^{10} \text{sgn}(X_{i,l} - X_{i,k}) \quad (2a)$$

$$\text{sgn}(X_{i,l} - X_{i,k}) = \begin{cases} 1 & X_{i,l} > X_{i,k} \\ 0 & X_{i,l} = X_{i,k} \\ -1 & X_{i,l} < X_{i,k} \end{cases}$$

where  $k$  and  $l$  represent the different year and  $l > k$ ,  $X_{i,l}$  and  $X_{i,k}$  represent the monthly value of the variable for the month  $i$  of the year  $k$  and  $l$ , respectively.

The  $\text{VAR}(S_i)$  is computed as:

$$\text{VAR}(S_i) = \frac{1}{18} [N_i(N_i - 1)(2N_i + 5) - \sum_{p=1}^{g_i} t_{i,p}(t_{i,p} - 1)(2t_{i,p} + 5)] \quad (2b)$$

where  $N_i$  is the length of the record for the month  $i$  (e.g. the 10 year data record in this study with  $N_i=10$ ),  $g_i$  is the number of equal-value data in month  $i$ ,  $t_{i,p}$  is the number of equal-value data in the  $p^{\text{th}}$  group for month  $i$ .

After obtaining the  $S_i$  and  $\text{VAR}(S_i)$ , the statistic  $S'$  and  $\text{VAR}(S')$  for the selected season (e.g. warm season is from May up to October and cold season is from November to April) can be summed as:

$$S' = \sum_{i=1}^M S_i \quad (2c)$$

239  $VAR(S') = \sum_{i=1}^M VAR(S_i)$  (2d)

240 where M represents the number of months in the selected season, e.g. M is 12 for the full year, and M is 6  
241 for the warm and cold seasons.

242 Subsequently, the Z metric can be computed as:

243 
$$Z = \begin{cases} \frac{S'-1}{\sqrt{Var(S')}} & \text{if } S' > 0 \\ 0 & \text{if } S' = 0 \\ \frac{S'+1}{\sqrt{Var(S')}} & \text{if } S' < 0 \end{cases}$$
 (2e)

244 If the statistics Z is positive (negative) and its absolute value is greater than  $Z_{1-\alpha/2}$  (here  $\alpha = 0.05$ ,  $Z_{1-\alpha/2} =$   
245 1.96), the trend of the time series is regarded as upward (downward) at the significance level of  $\alpha$ . Otherwise,  
246 we accept the hypothesis that no significant trend is found.

247 If the trend shows upward or downward, we will further estimate the slope (change per unit time) with Sen's  
248 method (Sen, 1968). The slopes of each month can be calculated as:

249  $Q_i = \frac{X_{i,l} - X_{i,k}}{l-k}$  (2f)

250 Then rank all the individual slopes ( $Q_i$ ) for all months and find the median, which is considered as the  
251 seasonal Kendall slope estimate.

### 252 3.3 Comparison metrics

253 The metrics used to evaluate the accuracy of the upscaled SM are the bias [ $m^3 m^{-3}$ ], RMSE [ $m^3 m^{-3}$ ], and  
254 unbiased RMSE (ubRMSE [ $m^3 m^{-3}$ ]), which can be formulated as:

256  $Bias = \frac{\sum_{t=1}^M (\theta_t^{tru} - \bar{\theta}_t^{ups})}{M}$  (3a)

257  $RMSE = \sqrt{\frac{\sum_{t=1}^M (\theta_t^{tru} - \bar{\theta}_t^{ups})^2}{M}}$  (3b)

258  $ubRMSE = \sqrt{RMSE^2 - BIAS^2}$  (3c)

259 where  $\theta_t^{tru}$  represents the SM that is considered as the ground truth, and  $\bar{\theta}_t^{ups}$  represents the upscaled SM.

260 The closer the metric is to zero, the more accurate the estimation is.

261 The metric used to assess the correlation between two time series is the Nash-Sutcliffe efficiency coefficient  
262 (NSE [-]), expressed by:

263  $NSE = 1 - \frac{\sum_{t=1}^n (\theta_t^{tru} - \bar{\theta}_t^{ups})^2}{\sum_{t=1}^n (\theta_t^{tru} - \bar{\theta}_t^{tru})^2}$  (4)

264 The value of the NSE ranges from  $-\infty$  to 1, and the closer the metric is to 1, the better the match of the  
265 estimated SM with the reference ( $\theta_t^{tru}$ ).

266 The metrics used to define the most representative SM time series (i.e. the best upscaled SM) is the  
267 comprehensive evaluation criterion (CEC [-]) obtained by combining the mean relative difference (MRD [-

268 ]) and standard deviation of the relative difference ( $\sigma(RD)$  [-]) (Jacobs et al., 2004). Detailed description of

269 above mentioned three metrics are given in Appendix B.3. It should be noted that the  $\theta_{t,i}^{obs}$  and  $\bar{\theta}_t^{obs}$  in Eqs.



270 (B4) and (B5) represent the upscaled SM using four different methods and their average when using the *CEC*  
271 to determine the best upscaled SM. The most representative time series is identified by the lowest *CEC* value.

### 272 **3.4 Preprocessing of model-based soil moisture products**

273 The performance of the ERA5-land, MERRA2, and GLDAS Noah SM products are assessed using the  
274 upscaled SM data of the Maqu and Shiquanhe networks for a 10-year period. The corresponding regional-  
275 scale SM for each product has been obtained by averaging the data from all the grid cells falling in the  
276 respective network areas. The numbers of grid cells covering the Maqu and Shiquanhe networks are 77 and  
277 20 for the ERA5-land product, 12 and 4 for the GLDAS Noah product, and only one for the MERRA2  
278 product. For the ERA5-land and MERRA2 products the data available at hourly and 3-hourly time steps are  
279 averaged to daily value and the units of GLDAS Noah SM is converted from  $\text{kg m}^{-2}$  to  $\text{m}^3 \text{m}^{-3}$ . Further it  
280 should be noted that the uppermost soil layer of the ERA5-land (0-7 cm), MERRA2 (0-5 cm), and GLDAS  
281 Noah (0–10 cm) SM products are assumed to match the *in situ* observations at depth of 5 cm considering the  
282 4 cm influence zone found under laboratory conditions for the 5TM sensor by Benninga et al. (2018).

## 283 **4 Results**

### 284 **4.1 Inter-comparison of soil moisture upscaling methods**

285 In this section, four upscaling methods (see Section 3.1) are inter-compared first with the input of the  
286 maximum number of available SM monitoring sites for a single year in the Maqu and Shiquanhe networks  
287 to find the most suitable upscaled SM that can best represent the areal conditions (i.e. ground truth,  $SM_{\text{truth}}$ ).  
288 Later on, the performance of the four upscaling methods is further investigated with the input of reducing  
289 number of SM monitoring sites to find the most suitable method for producing long-term (~10 year) upscaled  
290 SM for the Maqu and Shiquanhe networks.

291 Fig. 6 shows the time series of daily average SM for the Maqu and Shiquanhe networks produced by the four  
292 upscaling methods based on the maximum number of available SM monitoring sites (hereafter “ $SM_{\text{AA-max}}$ ”,  
293 “ $SM_{\text{VD-max}}$ ”, “ $SM_{\text{TS-max}}$ ”, and “ $SM_{\text{ATI-max}}$ ”). Two different periods are selected for the two networks due to the  
294 fact that the number of available monitoring sites reaches the maximum in different periods for the two  
295 networks, e.g. 17 sites for Maqu between November 2009 and October 2010 and 12 sites for Shiquanhe  
296 between August 2018 and July 2019, respectively (see Tables A2 and A4 in the Appendix A). For the Maqu  
297 network, the  $SM_{\text{AA-max}}$ ,  $SM_{\text{VD-max}}$ , and  $SM_{\text{TS-max}}$  are comparable to each other, while the  $SM_{\text{ATI-max}}$  deviates  
298 substantially during the winter (between December and February) and summer periods (between June and  
299 August). On the other hand, the  $SM_{\text{ATI-max}}$  for the Shiquanhe network is comparable to  $SM_{\text{AA-max}}$  and  $SM_{\text{VD-}}$   
300  $_{\text{max}}$ , while  $SM_{\text{TS-max}}$ 's behavior is clearly different from the others. It seems that the ATI method performs  
301 better in the Shiquanhe network due to the existence of a stronger relationship between  $\tau$  and  $\theta$  in the desert  
302 ecosystem.

303 Table B1 lists the values of  $MRD$  (see Eq. (B4) in Appendix B),  $\sigma(RD)$  (Eq. (B3)), and  $CEC$  (Eq. (B6))  
304 calculated for the upscaled SM produced by the four upscaling methods. The  $CEC$  is used here to determine  
305 the most suitable upscaled SM that can best represent the areal conditions for the two networks. It can be  
306 found that the  $SM_{AA-max}$  yields consistently the lowest  $CEC$  values for both networks, indicating that the  
307  $SM_{AA-max}$  can be used to represent actual areal conditions, which will thus be regarded as the ground truth for  
308 following analysis (i.e.  $SM_{truth}$ ). The arithmetic average of the dense *in situ* measurements was also used as  
309 the ground truth in other studies (Qin et al., 2013; Su et al., 2013) and found to yield reliable results by van  
310 der Velde et al. (2021).

311 As shown in Tables A2 and A4 (see Appendix A), the number of available SM monitoring sites decreased as  
312 time progressed. There are only three (i.e. CST05, NST01, and NST03) and four (i.e. SQ02, SQ03, SQ06,  
313 and SQ14) monitoring sites that provided more than nine years of *in situ* SM measurement data for the Maqu  
314 and Shiquanhe networks, respectively (see Tables 2 and 3). This indicates that the minimum number of  
315 available monitoring sites can be used to produce the long-term (~10 year) consistent upscaled SM are three  
316 and four for the Maqu and Shiquanhe networks, respectively. Fig. 7 shows the daily average SM time series  
317 produced by the four upscaling methods based on the minimum available monitoring sites (hereafter “AA-  
318 min”, “TS-min”, “VD-min”, and “ATI-min”). The  $SM_{truth}$  obtained by the AA-max is also shown for  
319 comparison purposes. For the Maqu network, the upscaled SM produced by the AA-min, VD-min, and TS-  
320 min generally capture well the  $SM_{truth}$  variations, while the upscaled SM of the ATI-min shows dramatic  
321 deviations. Similarly, the upscaled SM produced by the AA-min and VD-min are consistent with the  $SM_{truth}$   
322 for the Shiquanhe network with slight overestimations, while significant deviations are noted for the upscaled  
323 SM of the TS-min and ATI-min. Table B2 lists the error statistics (e.g. Bias, RMSE, ubRMSE, and NSE)  
324 computed between the upscaled SM produced by these four upscaling methods with the input of the minimum  
325 available sites and the  $SM_{truth}$ . The upscaled SM produced by the AA-min shows better performance for both  
326 networks as indicated by the lower RMSE and higher NSE values in comparison to the other three upscaling  
327 methods.

328 Apart from the maximum and minimum number of available SM monitoring sites mentioned above, there  
329 are about 14, 10, 8, and 6 available monitoring sites during different time spans for the Maqu network, and  
330 for the Shiquanhe network are about 11, 10, 6, and 5 available monitoring sites (see Tables A2 and A4 in the  
331 Appendix A). Fig. B2 shows the radar diagram of error statistics (i.e. RMSE and NSE) computed between  
332 the  $SM_{truth}$  and the upscaled SM produced by the four upscaling methods for different numbers of available  
333 monitoring sites. For the Maqu network, the performances of the AA and VD methods are better than the TS  
334 and ATI methods as indicated by smaller RMSEs and higher NSEs for all the estimations. A similar  
335 conclusion can be drawn for the Shiquanhe network, while the performance of the ATI method is largely  
336 improved when the number of available monitoring sites is not less than 10. It is interesting to note that the  
337 upscaled SM produced by the AA-min is comparable to those obtained with more sites (e.g. 10 sites) as  
338 indicated by comparable RMSE and NSE values for both networks. It indicates that the AA-min is suitable  
339 to produce long-term (~10 years) upscaled SM for both networks, which yield RMSEs of 0.022 and 0.011

340  $\text{m}^3 \text{m}^{-3}$  for the Maqu and Shiquanhe networks in comparison to the  $\text{SM}_{\text{truth}}$  produced by the AA-max based  
341 on the maximum available monitoring sites.

## 342 **4.2 Long-term analysis of upscaled soil moisture measurements**

343 In this section, the AA-min is first adopted to produce the consecutive upscaled SM time series (hereafter  
344 “ $\text{SM}_{\text{AA-min}}$ ”) for approximately an 10-year period for the Maqu and Shiquanhe networks, respectively. In  
345 addition, the other time series of upscaled SM are produced by the AA method with input of all available SM  
346 monitoring sites regardless of the continuity (hereafter “ $\text{SM}_{\text{AA-valid}}$ ”), which is widely used to validate the  
347 various SM products (Dente et al. 2012a; Chen et al. 2013; Zheng et al. 2018b) for short periods (e.g.  $\leq 2$   
348 years). This method may, however, leads to inconsistent SM time series for a long-term period due to the fact  
349 that the number of available sites is different in distinct periods (see Tables A2 and A4 in the Appendix A).  
350 Trend analyses (see Section 3.2) are applied to both  $\text{SM}_{\text{AA-min}}$  and  $\text{SM}_{\text{AA-valid}}$  to investigate the impact of  
351 changes of available SM monitoring sites on the long-term (i.e. 10-year) trend.

352 Fig. 8a shows the time series of  $\text{SM}_{\text{AA-min}}$  and  $\text{SM}_{\text{AA-valid}}$  along with the daily precipitation data for the Maqu  
353 network during the period between May 2009 and May 2019. Both two time series of the SM show similar  
354 seasonality with low values in winter due to frozen soils and high values in summer due to rainfall (see  
355 subplot of Fig. 8a). Deviations can be found between the  $\text{SM}_{\text{AA-min}}$  and  $\text{SM}_{\text{AA-valid}}$  especially for the period  
356 between 2014 and 2019, whereby the  $\text{SM}_{\text{AA-valid}}$  tends to produce smaller SM values in the warm season. Fig.  
357 9a shows further the Mann Kendall trend test and Sen’s slope estimate for the  $\text{SM}_{\text{AA-min}}$ ,  $\text{SM}_{\text{AA-valid}}$ , and  
358 precipitation of the Maqu network area for the full year, warm seasons, and cold seasons in a 10-year period.  
359 As described in Section 3.2, the time series would present a monotonous trend if the absolute value of  
360 statistics  $Z$  is greater than a critical value, i.e.  $Z_{0.05} = 1.96$  in this study. The results show that there is not  
361 significant trend found for both precipitation and  $\text{SM}_{\text{AA-min}}$  time series, while the  $\text{SM}_{\text{AA-valid}}$  shows a drying  
362 trend with a Sen’s slope of -0.008 for warm seasons. The drying trend of the  $\text{SM}_{\text{AA-valid}}$  is caused by the  
363 change of available SM monitoring sites (see Table A2). Specifically, several monitoring sites (e.g. NST11-  
364 NST15) located in the wetter area were damaged since 2013, and four new monitoring sites (i.e. NST21-  
365 NST25) were installed in the drier area in 2015 (see Table 2), which affects the trend of the  $\text{SM}_{\text{AA-valid}}$ .

366 Fig. 8b shows the time series of the  $\text{SM}_{\text{AA-min}}$  and  $\text{SM}_{\text{AA-valid}}$  along with the daily precipitation data for the  
367 Shiquanhe network during the period between August 2010 and August 2019. Both time series of the SM  
368 display a similar seasonality as found for the Maqu network (see subplot of Fig. 8b). However, obvious  
369 deviations can be noticed for the inter-annual variations, and the  $\text{SM}_{\text{AA-valid}}$  tends to produce larger values  
370 before 2014 but smaller values since then. The Mann Kendall trend test and Sen’s slope estimate for the  
371  $\text{SM}_{\text{AA-min}}$ ,  $\text{SM}_{\text{AA-valid}}$ , and precipitation time series of the Shiquanhe network area are shown in Fig. 9b. The  
372  $\text{SM}_{\text{AA-min}}$  demonstrates a wetting trend with a Sen’s slope of 0.003, while an opposite drying trend is found  
373 for the  $\text{SM}_{\text{AA-valid}}$  due to a change in number of available SM monitoring sites (see Table A4) similar to the  
374 results from the Maqu network. Specifically, several monitoring sites (e.g. SQ11 and SQ12) located in the

375 wetter area were damaged around 2014, and five new monitoring sites (i.e. SQ17-21) were installed in the  
376 drier area in 2016 (see Table 3).

377 In summary, the  $SM_{AA-valid}$  is likely affected by the change of available SM monitoring sites over time that  
378 leads to inconsistent trend with the  $SM_{AA-min}$ . This indicates that the  $SM_{AA-min}$  is superior to the  $SM_{AA-valid}$  for  
379 the production of the long-term consistent upscaled SM time series.

#### 380 **4.3 Application of the long-term upscaled soil moisture to validate the model-based products**

381 In this section, the long-term upscaled SM time series (i.e.  $SM_{AA-min}$ ) produced for the two networks are  
382 applied to validate the reliability of three model-based SM products, i.e. ERA5-land, MERRA2, and GLDAS  
383 Noah, to demonstrate the uniqueness of this dataset for validating existing reanalysis datasets for a long term  
384 period (~10 years). Since the ERA5-land product provides only total volumetric soil water content, the period  
385 when the soil is subject to freezing and thawing (i.e. November-April) is excluded for this evaluation.

386 Fig. 10a shows the time series of  $SM_{AA-min}$  and daily average SM data derived from the three products for the  
387 Maqu network during the period between May 2009 and May 2019. The error statistics, i.e. bias and RMSE,  
388 computed between the three products and the  $SM_{AA-min}$  for both warm (May-October) and cold seasons  
389 (November-April) are given in Table 5. Although the three products generally capture the seasonal variations  
390 of the  $SM_{AA-min}$ , the magnitude of the temporal SM variability is underestimated. Both GLDAS Noah and  
391 MERRA2 products underestimate the SM measurements during the warm season leading to biases of about  
392  $-0.112$  and  $-0.113 \text{ m}^3 \text{ m}^{-3}$ , respectively. This may be due to the fact that the LSMs adopted for producing  
393 these products do not consider the impact of vertical soil heterogeneity caused by organic matter contents  
394 that is widely present in the soil Tibetan surface (Chen et al., 2013; Zheng et al., 2015a). In addition, the  
395 MERRA2 product overestimates the SM measurements during the cold season with bias of about  $0.006 \text{ m}^3$   
396  $\text{m}^{-3}$ . The ERA5-land product is able to capture the magnitude of  $SM_{AA-min}$  dynamics in the warm season but  
397 has a larger volatility and yields a RMSE of about  $0.067 \text{ m}^3 \text{ m}^{-3}$ . The trend analysis for the three model-based  
398 SM products are shown in Fig. 9a as well. All three products do not show significant trend in warm seasons  
399 as the  $SM_{AA-min}$ , while the GLDAS Noah and MERRA2 products show a wetting trend in cold seasons that  
400 is in disagreement with the  $SM_{AA-min}$  trend.

401 Fig. 10b shows the time series of  $SM_{AA-min}$  and daily SM data derived from the three products for the  
402 Shiquanhe network area during the period between August 2010 and August 2019, and the corresponding  
403 error statistics are given in Table 5 as well. Although the three products generally capture the seasonal  
404 variations of the  $SM_{AA-min}$ , both GLDAS Noah and MERRA2 products overestimate the  $SM_{AA-min}$  during the  
405 entire study period leading to positive biases, and also positive bias (about  $0.002 \text{ m}^3 \text{ m}^{-3}$ ) is found in the  
406 ERA5-land product for the warm season. The trend analyses for the three SM products are also shown in Fig.  
407 9b. Both the ERA5-land and MERRA2 products are able to reproduce the wetting trend found for the  $SM_{AA-}$   
408  $min$ , while the GLDAS Noah product is not able to capture the trend.

409 In summary, the currently model-based SM products do not provide a reliable representation of the trend and  
410 the dynamics of measured SM on the long-term (~10 years) in the grassland and desert ecosystems that  
411 dominate the Tibetan landscape.

## 412 **5 Discussion**

413 As shown in previous sections, the number of available SM monitoring sites in the Tibet-Obs generally  
414 changes with time. For instance, several monitoring sites of the Maqu network located in the wetter area were  
415 damaged since 2013, and four new monitoring sites were installed in the drier area in 2015 that affects the  
416 trend of SM time series (i.e.  $SM_{AA-valid}$  shown in Section 4.2). On the other hand, the 10-year upscaled SM  
417 data (i.e.  $SM_{AA-min}$ ) produced in this study utilizing three and four monitoring sites with long-term continuous  
418 measurements would yield RMSEs of about 0.022 and 0.011  $m^3 m^{-3}$  for the Maqu and Shiquanhe networks,  
419 respectively (see Section 4.1). Therefore, to provide a higher-quality continuous SM time series for the future,  
420 it is necessary to find an appropriate strategy to maintain the monitoring sites of Tibet-Obs. This section  
421 discusses the possible strategies with the Maqu and Shiquanhe networks as examples.

422 At first, a sensitivity analysis is conducted to quantify the impact of the number of monitoring sites on the  
423 regional SM estimate. The SM time series described in Section 4.1 (i.e. 11/2009-10/2010 for the Maqu  
424 network and 8/2018-7/2019 for the Shiquanhe network) is used to test the sensitivity, and there are in total  
425 17 and 12 available monitoring sites for the Maqu and Shiquanhe networks, respectively. Taking the Maqu  
426 network as an example, we randomly pick different numbers of sites from 1 to 16 of the 17 sites to make up  
427 different combinations, and then compute the RMSEs of the averaged SM obtained with these combinations  
428 (Famiglietti et al., 2008; Zhao et al., 2013). These RMSEs are further grouped into nine levels ranging from  
429 0.004 to 0.02  $m^3 m^{-3}$ , and the percentage of the combinations falling into each level is summarized in Table  
430 6. In general, the percentage increases with increasing number of monitoring sites at any RMSE levels. It can  
431 be noted that more than 50% of combinations are able to comply with the RMSE requirement of 0.004  $m^3$   
432  $m^{-3}$  if the number of available monitoring sites are 16 and 11 in the Maqu and Shiquanhe networks,  
433 respectively. If the number of available monitoring sites are more than 13 and 6 in the Maqu and Shiquanhe  
434 networks, there are about 60% of combinations with 13 sites (6 sites ) are able to comply with the RMSE  
435 requirement of 0.01  $m^3 m^{-3}$ . For an RMSE of 0.02  $m^3 m^{-3}$ , more than 50% of combinations complies with  
436 this requirement if the number of available monitoring sites is more than 7 and 3 for the two networks,  
437 respectively. In summary, the number of monitoring sites required to maintain current networks depends on  
438 the defined RMSE requirement.

439 As shown in Section 4.1, the usage of a minimum number of sites (i.e. three for Maqu and four for Shiquanhe)  
440 with about 10-year continuous measurements yields RMSEs of 0.022 and 0.011  $m^3 m^{-3}$  for the Maqu and  
441 Shiquanhe networks, respectively. Since there are still 12 monitoring sites providing SM measurements for  
442 both networks until 2019 (see Tables 2 and 3), it is possible to decrease the RMSEs when the selected  
443 permanent monitoring sites are appropriately determined. For the Shiquanhe network, the optimal strategy is  
444 to keep the current 12 monitoring sites, which is exactly the combination used in Section 4.1. For the Maqu

445 network, it can be found that there is about 3.52% of combinations with 12 sites could yield the minimum  
446 RMSE of  $0.006 \text{ m}^3 \text{ m}^{-3}$  (see Table 6). In order to find the optimal combination with 12 sites for the Maqu  
447 network, all the possible combinations (i.e. the number of 6188) are ranked by RMSE values from the  
448 smallest to largest, and Table 7 lists the examples of ranking 1-5<sup>th</sup> and 95-100<sup>th</sup>. It can be noted that the 100<sup>th</sup>  
449 combination contains the largest number of currently available monitoring sites (i.e. 7 sites including CST03,  
450 CST05, NST01, NST03, NST05, NST06, and NST10) with a RMSE of less than  $0.006 \text{ m}^3 \text{ m}^{-3}$ . Therefore,  
451 the 100<sup>th</sup> combination of 12 monitoring sites (as shown in Table 7) is suggested for the Maqu network.  
452 In summary, it is suggested to maintain the current 12 monitoring sites for the Shiquanhe network, while for  
453 the Maqu network it is suggested to restore five old monitoring sites, i.e. CST02, NST11, NST13, NST14,  
454 and NST15.

## 455 **6 Data availability**

456 The 10-year (2009-2019) surface SM dataset is freely available from the 4TU.ResearchData repository at  
457 <https://doi.org/10.4121/12763700.v7> (Zhang et al., 2020). The original *in situ* SM data, the upscaled SM data,  
458 and the supplementary data are stored in .xlsx files. A user guide document is given to introduce the content  
459 of the dataset, the status of the Tibet-Obs, and the online dataset utilized in the study.

## 460 **7 Conclusions**

461 In this paper, we report on the status of the Tibet-Obs and present the long-term *in situ* SM and spatially  
462 upscaled SM dataset for the period 2009-2019. In general, the number of available SM monitoring sites  
463 decreased over time due to damage of sensors. Until 2019, there are only three and four sites that provide an  
464 approximately 10-year consistent SM time series for the Maqu and Shiquanhe networks, respectively.  
465 Comparisons between four upscaling methods, i.e. arithmetic averaging (AA), Voronoi diagram (VD), time  
466 stability (TS), and apparent thermal inertia (ATI), show that the AA method with input of the maximum  
467 number of available SM monitoring sites (AA-max) can be used to represent the actual areal SM conditions  
468 ( $SM_{\text{truth}}$ ). The arithmetic average of the three and four monitoring sites with long-term continuous  
469 measurements (AA-min) are found to be most suitable to produce the upscaled SM dataset for the period  
470 2009-2019, which yields RMSEs of 0.022 and  $0.011 \text{ m}^3 \text{ m}^{-3}$  for the Maqu and Shiquanhe networks in  
471 comparison to the  $SM_{\text{truth}}$ .

472 Trend analysis of the approximately 10-year upscaled SM time series produced by the AA-min ( $SM_{\text{AA-min}}$ )  
473 shows that the Shiquanhe network in the western part of the TP is getting wet while no significant trend is  
474 found for the Maqu network in the east. The usage of all the available monitoring sites each year leads to  
475 inconsistent time series of SM that cannot capture the trend of  $SM_{\text{AA-min}}$  reliably. Comparisons between the  
476  $SM_{\text{AA-min}}$  and the model-based SM products from the ERA5-land, GLDAS Noah, and MERRA2 further  
477 demonstrate that current model-based SM products still show deficiencies in representing the trend and the  
478 dynamics of the SM measured on the TP. Moreover, strategies for maintaining the Tibet-Obs are provided,

479 and it is suggested to maintain currently 12 operational sites for the Shiquanhe network, while for the Maqu  
480 network it is suggested to restore five old sites.

481 The 10-year (2009-2019) surface SM dataset presented in this paper includes the 15-min *in situ* measurements  
482 taken at a depth of 5 cm collected from three regional-scale networks (i.e. Maqu, Naqu, and Ngari including  
483 Ali and Shiquanhe) of the Tibet-Obs, and the spatially upscaled SM datasets produced by the AA-min for  
484 the Maqu and Shiquanhe networks. This dataset is valuable for calibrating/validating long-term satellite- and  
485 model-based SM products, evaluation of SM upscaling methods, development of data fusion methods, and  
486 quantifying the coupling of SM with precipitation at 10-year scale.

#### 487 **Author contribution**

488 Pei Zhang, Donghai Zheng, Rogier van der Velde and Zhongbo Su designed the framework of this work. Pei  
489 Zhang performed the computations and data analysis, and written the manuscript. Donghai Zheng, Rogier  
490 van der Velde and Zhongbo Su supervised the progress of this work and provided critical suggestions, and  
491 revised the manuscript. Zhongbo Su and Jun Wen designed the setup of Tibet-Obs, Yijian Zeng, XinWang  
492 and Zuoliang Wang involved in maintaining the Tibet-Obs and downloading the original measurements. Pei  
493 Zhang, Zuoliang Wang, and Jiali Chen organized the data.

#### 494 **Competing interests**

495 The authors declare that they have no conflict of interest.

#### 496 **Acknowledgments**

497 This study was supported by the Strategic Priority Research Program of Chinese Academy of Sciences (Grant  
498 No. XDA20100103) and National Natural Science Foundation of China (Grant No. 41971308, 41871273).

#### 499 **Reference**

- 500 Albergel, C., Dutra, E., Munier, S., Calvet, J.-C., Muñoz Sabater, J., Rosnay, P. and Balsamo, G.: ERA-5  
501 and ERA-Interim driven ISBA land surface model simulations: Which one performs better?,  
502 Hydrology and Earth System Sciences, 22, doi:10.5194/hess-22-3515-2018, 2018.
- 503 Benninga, H.-J. F., Carranza, C. D. U., Peziz, M., van Santen, P., van der Ploeg, M. J., Augustijn, D. C. M.  
504 and van der Velde, R.: The Raam regional soil moisture monitoring network in the Netherlands,  
505 Earth System Science Data, 10(1), 61–79, doi:10.5194/essd-10-61-2018, 2018.
- 506 Bi, H. and Ma, J.: Evaluation of simulated soil moisture in GLDAS using in-situ measurements over the  
507 Tibetan Plateau, International Geoscience and Remote Sensing Symposium (IGARSS), 2015-  
508 Novem, 4825–4828, doi:10.1109/IGARSS.2015.7326910, 2015.
- 509 Chen, Y., Yang, K., Qin, J., Zhao, L., Tang, W. and Han, M.: Evaluation of AMSR-E retrievals and GLDAS  
510 simulations against observations of a soil moisture network on the central Tibetan Plateau, Journal  
511 of Geophysical Research Atmospheres, 118(10), 4466–4475, doi:10.1002/jgrd.50301, 2013.
- 512 Cheng, M., Zhong, L., Ma, Y., Zou, M., Ge, N., Wang, X. and Hu, Y.: A study on the assessment of multi-  
513 source satellite soil moisture products and reanalysis data for the Tibetan Plateau, Remote Sensing,

514 11(10), doi:10.3390/rs11101196, 2019.

515 Colliander, A., Jackson, T. J., Bindlish, R., Chan, S., Das, N., Kim, S. B., Cosh, M. H., Dunbar, R. S., Dang,  
516 L., Pashaian, L., Asanuma, J., Aida, K., Berg, A., Rowlandson, T., Bosch, D., Caldwell, T., Caylor,  
517 K., Goodrich, D., al Jassar, H., Lopez-Baeza, E., Martínez-Fernández, J., González-Zamora, A.,  
518 Livingston, S., McNairn, H., Pacheco, A., Moghaddam, M., Montzka, C., Notarnicola, C., Niedrist,  
519 G., Pellarin, T., Prueger, J., Pulliainen, J., Rautiainen, K., Ramos, J., Seyfried, M., Starks, P., Su,  
520 Z., Zeng, Y., van der Velde, R., Thibeault, M., Dorigo, W., Vreugdenhil, M., Walker, J. P., Wu, X.,  
521 Monerris, A., O'Neill, P. E., Entekhabi, D., Njoku, E. G. and Yueh, S.: Validation of SMAP surface  
522 soil moisture products with core validation sites, *Remote Sensing of Environment*, 191, 215–231,  
523 doi:10.1016/j.rse.2017.01.021, 2017.

524 Dente, L., Vekerdy, Z., Wen, J. and Su, Z.: Maqu network for validation of satellite-derived soil moisture  
525 products, *International Journal of Applied Earth Observation and Geoinformation*, 17, 55–65,  
526 doi:https://doi.org/10.1016/j.jag.2011.11.004, 2012a.

527 Dente, L., Su, Z. and Wen, J.: Validation of SMOS soil moisture products over the Maqu and Twente  
528 Regions, *Sensors (Switzerland)*, 12(8), 9965–9986, doi:10.3390/s120809965, 2012b.

529 Van doninck, J., Peters, J., De Baets, B., De Clercq, E. M., Ducheyne, E. and Verhoest, N. E. C.: The potential  
530 of multitemporal Aqua and Terra MODIS apparent thermal inertia as a soil moisture indicator,  
531 *International Journal of Applied Earth Observation and Geoinformation*, 13(6), 934–941,  
532 doi:https://doi.org/10.1016/j.jag.2011.07.003, 2011.

533 Famiglietti, J. S., Ryu, D., Berg, A. A., Rodell, M. and Jackson, T. J.: Field observations of soil moisture  
534 variability across scales, *Water Resources Research*, 44(1), 1–16, doi:10.1029/2006WR005804,  
535 2008.

536 Gao, S., Zhu, Z., Weng, H. and Zhang, J.: Upscaling of sparse in situ soil moisture observations by integrating  
537 auxiliary information from remote sensing, *International Journal of Remote Sensing*, 38(17), 4782–  
538 4803, doi:10.1080/01431161.2017.1320444, 2017.

539 Gilbert, Richland O, *Statistical Methods for Environmental Pollution Monitoring*, United States.  
540 https://www.osti.gov/biblio/7037501, 1987.

541 GMAO, Global Modeling and Assimilation Office: MERRA-2 tavg1\_2d\_Ind\_Nx: 2d,1-Hourly,Time-  
542 Averaged,Single-Level,Assimilation,Land Surface Diagnostics V5.12.4, Greenbelt, MD, USA,  
543 Goddard Earth Sciences Data and Information Services Center (GES DISC), 2015.

544 Jacobs, J. M., Mohanty, B. P., Hsu, E.-C. and Miller, D.: SMEX02: Field scale variability, time stability and  
545 similarity of soil moisture, *Remote Sensing of Environment*, 92(4), 436–446,  
546 doi:https://doi.org/10.1016/j.rse.2004.02.017, 2004.

547 Ju, F., An, R. and Sun, Y.: Immune evolution particle filter for soil moisture data assimilation, *Water*  
548 (Switzerland), 11(2), doi:10.3390/w11020211, 2019.

549 Kang, J., Jin, R., Li, X. and Zhang, Y.: Block Kriging With Measurement Errors: A Case Study of the Spatial  
550 Prediction of Soil Moisture in the Middle Reaches of Heihe River Basin, *IEEE Geoscience and*  
551 *Remote Sensing Letters*, 14(1), 87–91, doi:10.1109/LGRS.2016.2628767, 2017.

552 Li, C., Lu, H., Yang, K., Han, M., Wright, J. S., Chen, Y., Yu, L., Xu, S., Huang, X. and Gong, W.: The  
553 evaluation of SMAP enhanced soil moisture products using high-resolution model simulations and  
554 in-situ observations on the Tibetan Plateau, *Remote Sensing*, 10(4), 1–16, doi:10.3390/rs10040535,  
555 2018.

556 Liu, J., Chai, L., Lu, Z., Liu, S., Qu, Y., Geng, D., Song, Y., Guan, Y., Guo, Z., Wang, J. and Zhu, Z.:  
557 Evaluation of SMAP, SMOS-IC, FY3B, JAXA, and LPRM Soil moisture products over the  
558 Qinghai-Tibet Plateau and Its surrounding areas, *Remote Sensing*, 11(7), doi:10.3390/rs11070792,  
559 2019.

560 Mann, H. B.: Nonparametric Tests Against Trend, *Econometrica*, 13(3), 245–259, doi:10.2307/1907187,  
561 1945.

562 Moghaddam, M., Clewley, D., Silva, A. and Akbar, R.: The SoilSCAPE Network Multiscale In-situ Soil  
563 Moisture Measurements: Innovations in Network Design and Approaches to Upscaling in Support  
564 of SMAP, in *AGU Fall Meeting Abstracts*, vol. 2014, pp. IN11A-3599, online availbale from:  
565 https://ui.adsabs.harvard.edu/abs/2014AGUFMIN11A3599M, 2014.

566 Muñoz-Sabater, J., Dutra, E., Balsamo, G., Schepers, D., Albergel, C., Boussetta, S., Agustí-Panareda, A.,  
567 Zsoter, E., and Hersbach, H.: ERA5-Land: an improved version of the ERA5 reanalysis land  
568 component, *Joint ISWG and LSA-SAF Workshop IPMA*, Lisbon, 26–28, 2018.

569 Qin, J., Yang, K., Lu, N., Chen, Y., Zhao, L. and Han, M.: Spatial upscaling of in-situ soil moisture



570 measurements based on MODIS-derived apparent thermal inertia, *Remote Sensing of Environment*,  
571 138, 1–9, doi:10.1016/j.rse.2013.07.003, 2013.

572 Qin, J., Zhao, L., Chen, Y., Yang, K., Yang, Y., Chen, Z. and Lu, H.: Inter-comparison of spatial upscaling  
573 methods for evaluation of satellite-based soil moisture, *Journal of Hydrology*, 523, 170–178,  
574 doi:10.1016/j.jhydrol.2015.01.061, 2015.

575 Rodell, M., Houser, P. R., Jambor, U., Gottschalck, J., Mitchell, K., Meng, C.-J., Arsenault, K., Cosgrove,  
576 B., Radakovich, J., Bosilovich, M., Entin, J. K., Walker, J. P., Lohmann, D. and Toll, D.: The Global  
577 Land Data Assimilation System, *Bulletin of the American Meteorological Society*, 85(3), 381–394,  
578 doi:10.1175/BAMS-85-3-381, 2004.

579 Sen, P. K.: Estimates of the Regression Coefficient Based on Kendall's Tau, *Journal of the American*  
580 *Statistical Association*, 63(324), 1379–1389, doi:10.1080/01621459.1968.10480934, 1968.

581 Su, Z., Wen, J., Dente, L., Van Der Velde, R., Wang, L., Ma, Y., Yang, K. and Hu, Z.: The tibetan plateau  
582 observatory of plateau scale soil moisture and soil temperature (Tibet-Obs) for quantifying  
583 uncertainties in coarse resolution satellite and model products, *Hydrology and Earth System*  
584 *Sciences*, 15(7), 2303–2316, doi:10.5194/hess-15-2303-2011, 2011.

585 Su, Z., De Rosnay, P., Wen, J., Wang, L. and Zeng, Y.: Evaluation of ECMWF's soil moisture analyses using  
586 observations on the Tibetan Plateau, *Journal of Geophysical Research Atmospheres*, 118(11), 5304–  
587 5318, doi:10.1002/jgrd.50468, 2013.

588 Tarantola, A.: *Inverse Problem Theory and Methods for Model Parameter Estimation*, Society for Industrial  
589 and Applied Mathematics., 2005.

590 Topp, G. C., Davis, J. L. and Annan, A. P.: Electromagnetic determination of soil water content:  
591 Measurements in coaxial transmission lines, *Water Resources Research*, 16(3), 574–582,  
592 doi:https://doi.org/10.1029/WR016i003p00574, 1980.

593 Vachaud, G., Passerat De Silans, A., Balabanis, P. and Vauclin, M.: Temporal Stability of Spatially Measured  
594 Soil Water Probability Density Function1, *Soil Science Society of America Journal*, 49, 822–828,  
595 doi:10.2136/sssaj1985.03615995004900040006x, 1985.

596 Velde, R.: Soil moisture remote sensing using active microwaves and land surface modelling, 1 January.,  
597 2010.

598 van der Velde, R., Salama, M. S., Pellarin, T., Ofwono, M., Ma, Y. and Su, Z.: Long term soil moisture  
599 mapping over the Tibetan plateau using Special Sensor Microwave/Imager, *Hydrology and Earth*  
600 *System Sciences*, 18, 1323–1337, doi:10.5194/hess-18-1323-2014, 2014a.

601 van der Velde, R., Su, Z. and Wen, J.: Roughness determination from multi-angular ASAR Wide Swath  
602 mode observations for soil moisture retrieval over the Tibetan Plateau, *Proceedings of the European*  
603 *Conference on Synthetic Aperture Radar, EUSAR, Proceeding(August 2011)*, 163–165, 2014b.

604 van der Velde, R., Colliander, A., Peziz, M., Benninga, H.-J. F., Bindlish, R., Chan, S. K., Jackson, T. J.,  
605 Hendriks, D. M. D., Augustijn, D. C. M. and Su, Z.: Validation of SMAP L2 passive-only soil  
606 moisture products using upscaled in situ measurements collected in Twente, the Netherlands,  
607 *Hydrology and Earth System Sciences*, 25(1), 473–495, doi:10.5194/hess-25-473-2021, 2021.

608 Veroustraete, F., Li, Q., Verstraeten, W. W., Chen, X., Bao, A., Dong, Q., Liu, T. and Willems, P.: Soil  
609 moisture content retrieval based on apparent thermal inertia for Xinjiang province in China,  
610 *International Journal of Remote Sensing*, 33(12), 3870–3885, doi:10.1080/01431161.2011.636080,  
611 2012.

612 Wang, J., Ge, Y., Song, Y. and Li, X.: A Geostatistical Approach to Upscale Soil Moisture With Unequal  
613 Precision Observations, *IEEE Geoscience and Remote Sensing Letters*, 11(12), 2125–2129,  
614 doi:10.1109/LGRS.2014.2321429, 2014.

615 Wei, Z., Meng, Y., Zhang, W., Peng, J. and Meng, L.: Downscaling SMAP soil moisture estimation with  
616 gradient boosting decision tree regression over the Tibetan Plateau, *Remote Sensing of*  
617 *Environment*, 225(February), 30–44, doi:10.1016/j.rse.2019.02.022, 2019.

618 Yang, K., Chen, Y., He, J., Zhao, L., Lu, H. and Qin, J.: Development of a daily soil moisture product for the  
619 period of 2002–2011 in Mainland China., *Science China Earth Sciences*, doi:10.1007/s11430-019-  
620 9588-5, 2020.

621 Zeng, J., Li, Z., Chen, Q., Bi, H., Qiu, J. and Zou, P.: Evaluation of remotely sensed and reanalysis soil  
622 moisture products over the Tibetan Plateau using in-situ observations, *Remote Sensing of*  
623 *Environment*, 163, 91–110, doi:https://doi.org/10.1016/j.rse.2015.03.008, 2015.

624 Zeng, Y., Su, Z., Van Der Velde, R., Wang, L., Xu, K., Wang, X. and Wen, J.: Blending satellite observed,  
625 model simulated, and in situ measured soil moisture over Tibetan Plateau, *Remote Sensing*, 8(3),

626 1–22, doi:10.3390/rs8030268, 2016.

627 Zhang, P., Zheng, D., van der Velde, R., Wen, J., Zeng, Y., Wang, X., Wang, Z., Chen, J. and Su, Z.: A 10-

628 year (2009-2019) surface soil moisture dataset produced based on in situ measurements collected

629 from the Tibet-Obs. 4TU.ResearchData. Dataset. <https://doi.org/10.4121/12763700.v7>, 2020.

630 Zhang, Q., Fan, K., Singh, V. P., Sun, P. and Shi, P.: Evaluation of Remotely Sensed and Reanalysis Soil

631 Moisture Against In Situ Observations on the Himalayan-Tibetan Plateau, *Journal of Geophysical*

632 *Research: Atmospheres*, 123(14), 7132–7148, doi:10.1029/2017JD027763, 2018.

633 Zhao, H., Zeng, Y., Lv, S. and Su, Z.: Analysis of soil hydraulic and thermal properties for land surface

634 modeling over the Tibetan Plateau, *Earth System Science Data*, 10(2), 1031–1061,

635 doi:10.5194/essd-10-1031-2018, 2018.

636 Zhao, L., Yang, K., Qin, J., Chen, Y., Tang, W., Montzka, C., Wu, H., Lin, C., Han, M. and Vereecken, H.:

637 Spatiotemporal analysis of soil moisture observations within a Tibetan mesoscale area and its

638 implication to regional soil moisture measurements, *Journal of Hydrology*, 482, 92–104,

639 doi:10.1016/j.jhydrol.2012.12.033, 2013.

640 Zhao, W., Li, A., Jin, H., Zhang, Z., Bian, J. and Yin, G.: Performance evaluation of the triangle-based

641 empirical soil moisture relationship models based on Landsat-5 TM data and in situ measurements,

642 *IEEE Transactions on Geoscience and Remote Sensing*, 55(5), 2632–2645,

643 doi:10.1109/TGRS.2017.2649522, 2017.

644 Zheng, D., van der Velde, R., Su, Z., Wang, X., Wen, J., Booij, M. J., Hoekstra, A. Y. and Chen, Y.:

645 Augmentations to the Noah Model Physics for Application to the Yellow River Source Area. Part

646 I: Soil Water Flow, *Journal of Hydrometeorology*, 16(6), 2659–2676, doi:10.1175/JHM-D-14-

647 0198.1, 2015a.

648 Zheng, D., van der Velde, R., Su, Z., Wang, X., Wen, J., Booij, M. J., Hoekstra, A. Y. and Chen, Y.:

649 Augmentations to the Noah Model Physics for Application to the Yellow River Source Area. Part

650 II: Turbulent Heat Fluxes and Soil Heat Transport, *Journal of Hydrometeorology*, 16(6), 2677–2694,

651 doi:10.1175/JHM-D-14-0199.1, 2015b.

652 Zheng, D., van der Velde, R., Wen, J., Wang, X., Ferrazzoli, P., Schwank, M., Colliander, A., Bindlish, R.

653 and Su, Z.: Assessment of the SMAP Soil Emission Model and Soil Moisture Retrieval Algorithms

654 for a Tibetan Desert Ecosystem, *IEEE Transactions on Geoscience and Remote Sensing*, 56(7),

655 3786–3799, doi:10.1109/TGRS.2018.2811318, 2018a.

656 Zheng, D., Wang, X., van der Velde, R., Ferrazzoli, P., Wen, J., Wang, Z., Schwank, M., Colliander, A.,

657 Bindlish, R. and Su, Z.: Impact of surface roughness, vegetation opacity and soil permittivity on L-

658 band microwave emission and soil moisture retrieval in the third pole environment, *Remote Sensing*

659 *of Environment*, 209(November 2017), 633–647, doi:10.1016/j.rse.2018.03.011, 2018b.

660 Zheng, D., Wang, X., van der Velde, R., Schwank, M., Ferrazzoli, P., Wen, J., Wang, Z., Colliander, A.,

661 Bindlish, R. and Su, Z.: Assessment of Soil Moisture SMAP Retrievals and ELBARA-III

662 Measurements in a Tibetan Meadow Ecosystem, *IEEE Geoscience and Remote Sensing Letters*,

663 16(9), 1407–1411, doi:10.1109/lgrs.2019.2897786, 2019.

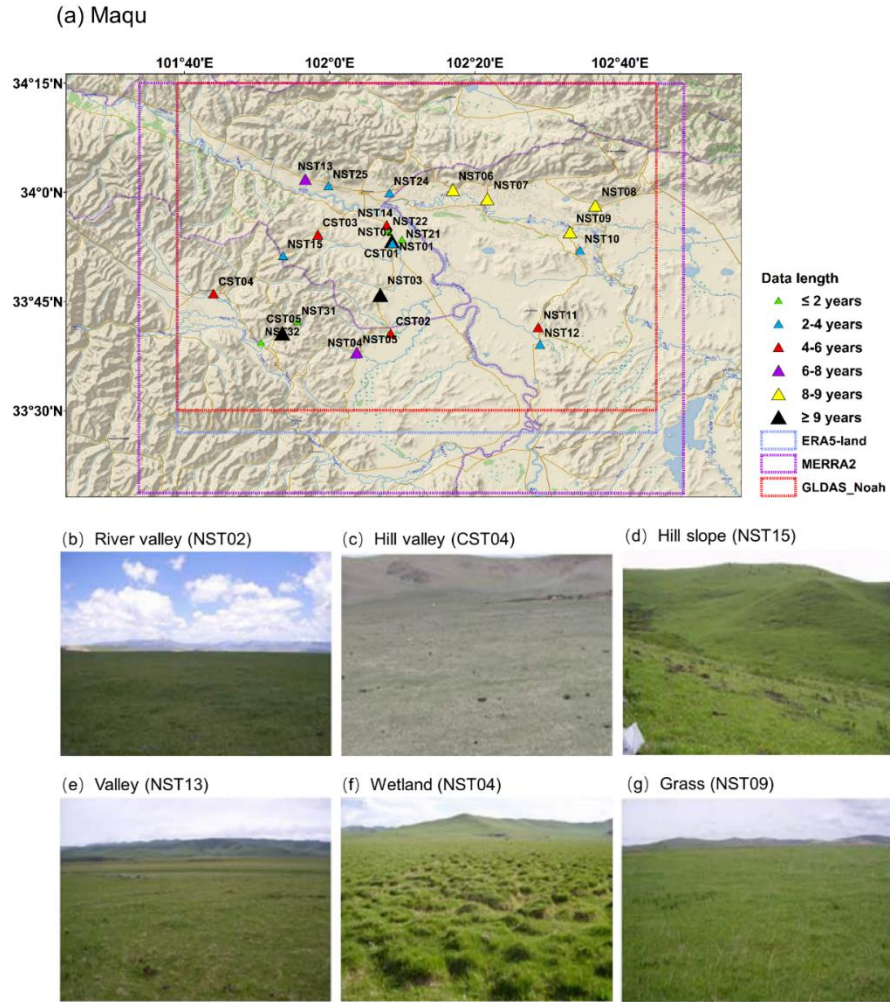
664



- \* CMA weather station
- Tibet-Obs network

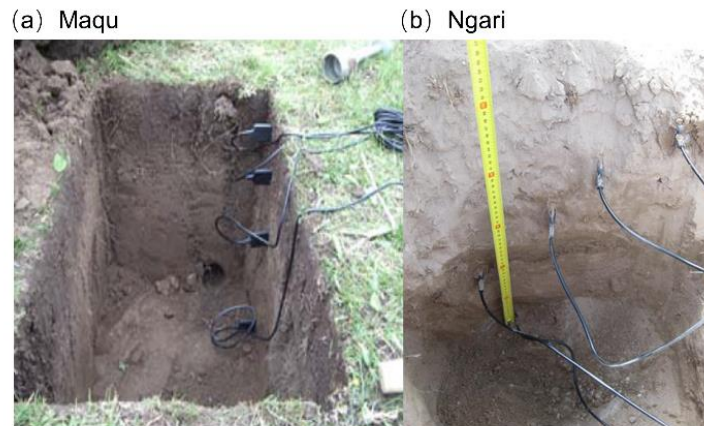
665

666 Fig. 1. Locations of the Tibet-Obs including Maqu, Naqu, and Ngari (including Ali and Shiquanhe) soil moisture  
 667 monitoring networks. The weather stations of Maqu and Shiquanhe operated by the China Meteorological  
 668 Administration (CMA) are also shown. (Base map is from Esri, Copyright: © Esri)



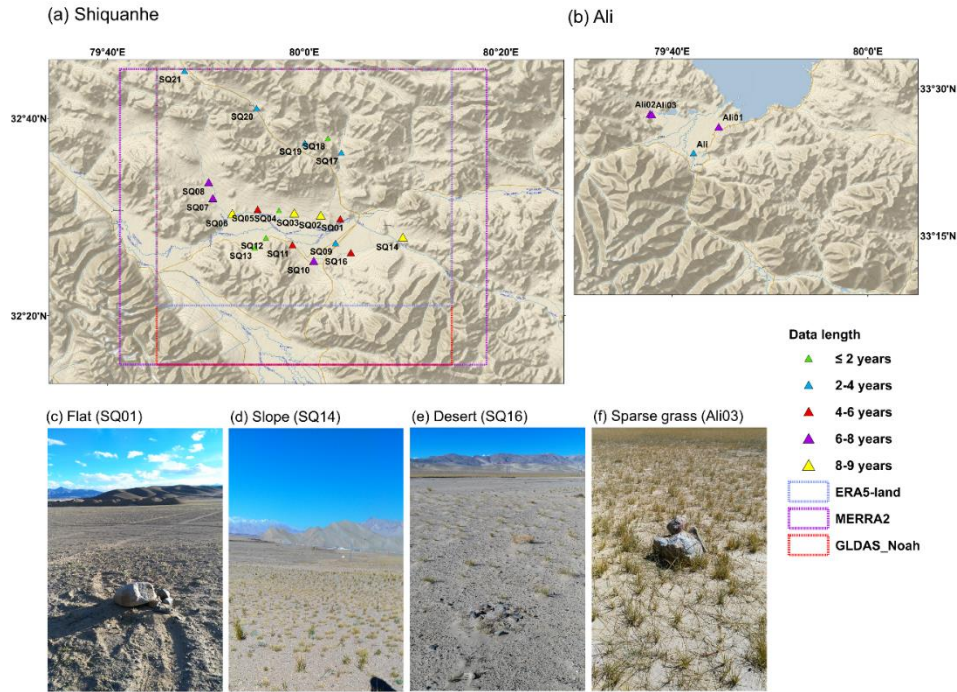
669

670 Fig. 2. (a) Overview of the Maqu monitoring network, and typical characteristics of topography and land cover  
 671 within the network: (b) river valley, (c) hill valley, (d) hill slope, (e) valley, (f) wetland and (g) grass. The colored  
 672 triangles in (a) represent different data lengths of surface SM measurements for each site, and the colored boxes  
 673 represent the coverage of selected model-based products. The site name in the bracket in (b)-(g) indicates the site  
 674 location for which the photograph is selected. (Base map copyright: ©2018 Garmin)



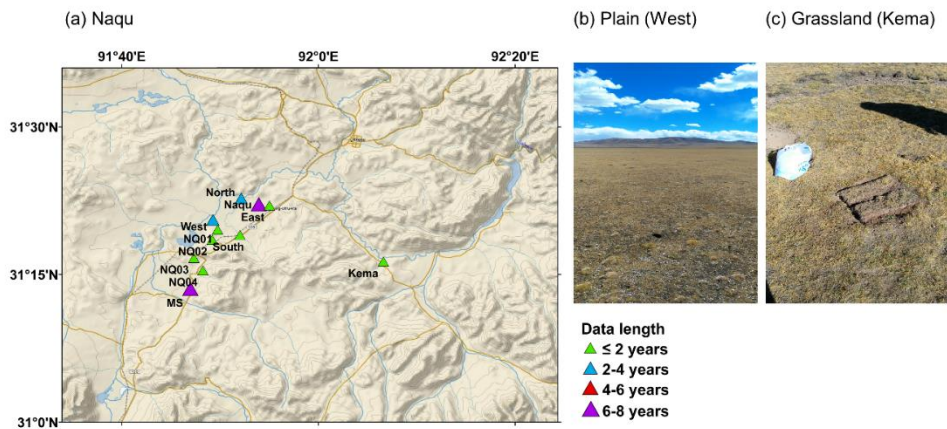
675

676 Fig. 3. Examples of typical installation of sensors in monitoring sites of (a) Maqu and (b) Ngari networks.



677

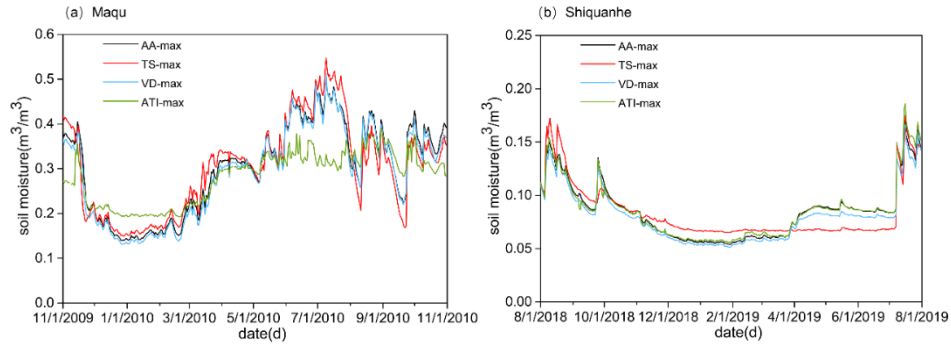
678 **Fig. 4. Overview of the Ngari monitoring network including (a) Shiquanhe and (b) Ali networks, and typical**  
 679 **characteristics of topography and land cover within the network: (c) flat, (d) slope, (e) desert, and (f) sparse grass.**  
 680 **The colored triangles in (a) and (b) represent different data lengths of surface SM measurements for each site,**  
 681 **and the colored boxes represent the coverage of selected model-based products. The site name in the bracket in**  
 682 **(c)-(f) indicates the site location for which the photograph is selected. (Base map copyright: ©2018 Garmin)**



683

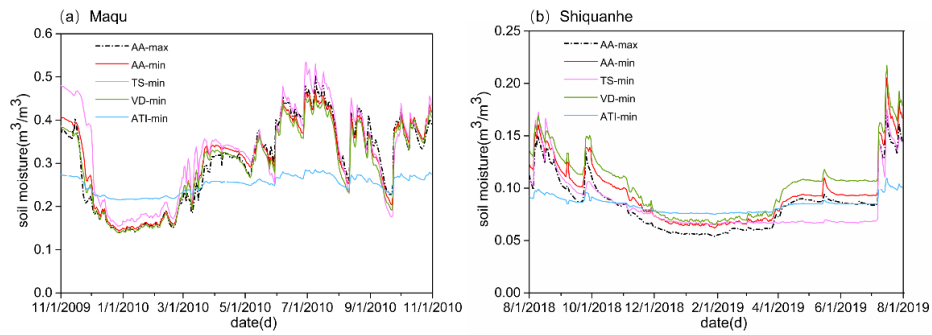
684 **Fig. 5. (a) Overview of the Naqu monitoring network, and typical characteristics of topography and land cover**  
 685 **within the network: (b) plain and (c) grassland. The colored triangles in (a) represent different data lengths of**  
 686 **surface SM measurements for each site. The site name in the bracket in (b) and (c) indicates the site location for**  
 687 **which the photograph is selected. (Base map copyright: ©2018 Garmin)**

688



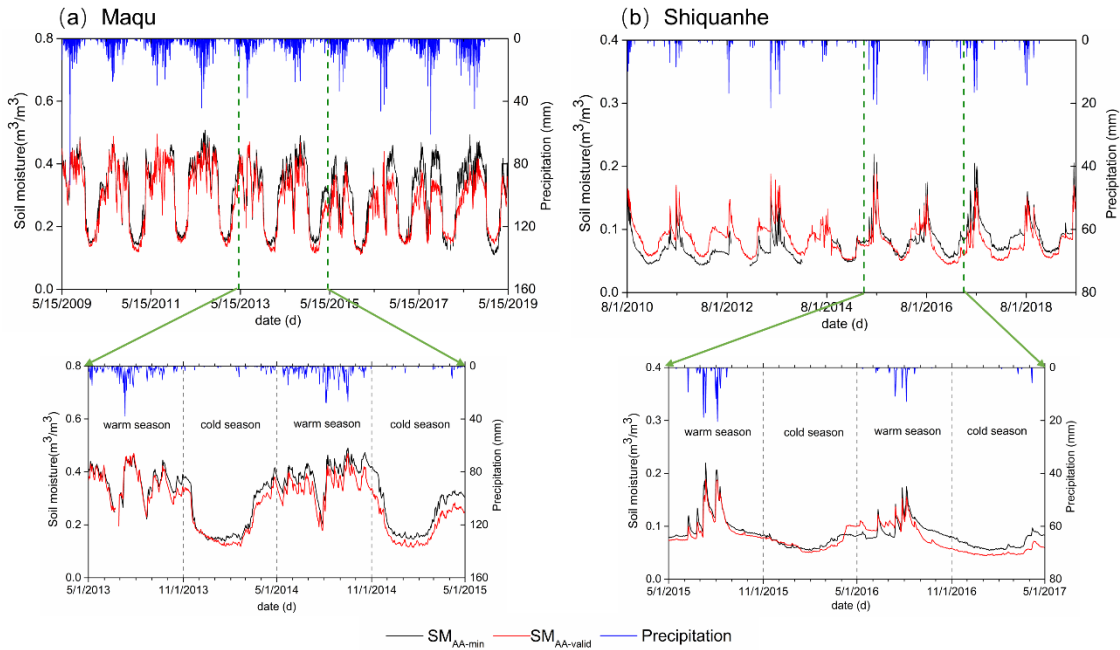
689

690 **Fig. 6. Comparisons of daily average SM for the (a) Maqu and (b) Shiquanhe networks produced by four upscaling**  
 691 **methods with input of the maximum number of available SM monitoring sites.**



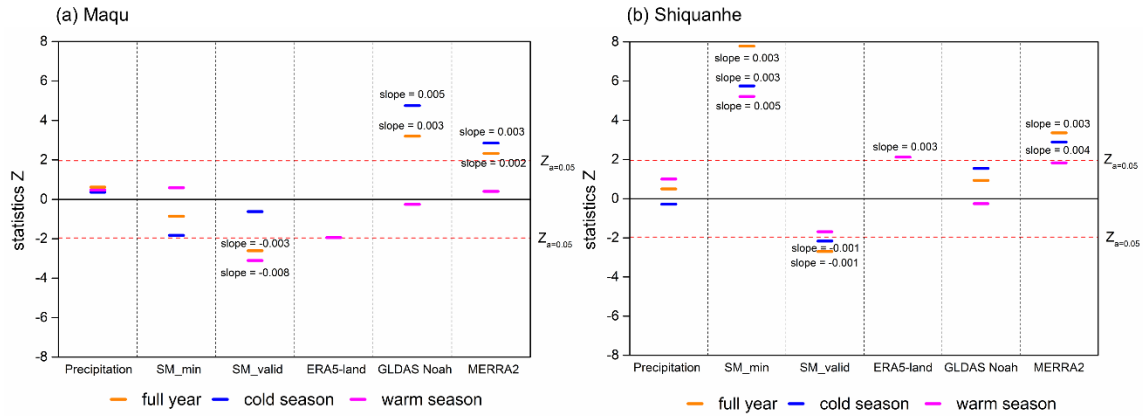
692

693 **Fig. 7. Comparisons of daily average SM for the (a) Maqu and (b) Shiquanhe networks produced by four upscaling**  
 694 **methods with input of the minimum number of available SM monitoring sites.**



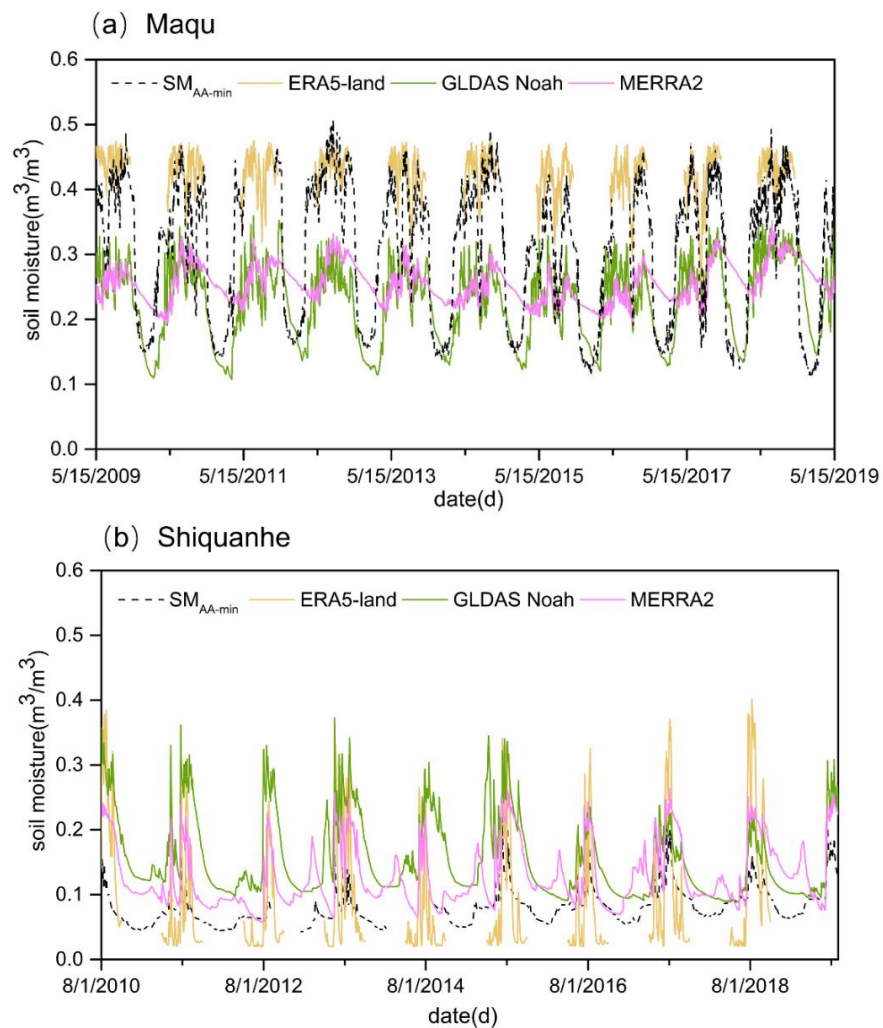
695

696 **Fig. 8. Time series of  $SM_{AA-min}$ ,  $SM_{AA-valid}$ , and precipitation for the (a) Maqu and (b) Shiquanhe networks for a**  
 697 **10-year period, the subplot highlights a 2-year period.**



698

699 **Fig. 9. Mann Kendall trend test and Sen's slope estimate for precipitation,  $SM_{AA-min}$ ,  $SM_{AA-valid}$ , and model-based**  
 700 **SM derived from the ERA5-land, GLDAS Noah, and MERRA2 for a 10-year period for the (a) Maqu and (b)**  
 701 **Shiquanhe networks.**



702

703 **Fig. 10. A 10-year time series of model-based SM derived from the ERA5-land, MERRA2, and GLDAS Noah**  
 704 **products and the upscaled SM ( $SM_{AA-min}$ ) for the (a) Maqu and (b) Shiquanhe networks.**

**Table 1. Summary of the main Tibet-Obs applications and corresponding findings.**

<b>Literature</b>	<b><i>In situ</i> data</b>	<b>Satellite- and/or model-based products</b>	<b>Key findings</b>
Dente et al. (2012a)	Maqu network, period between 2008 and 2009	LPRM AMSR-E SM product, ASCAT SM product	i) The weighted average of SM depended on the percentage spatial coverage strata can be regarded as the ground reference. ii) The AMSR-E and ASCAT products are able to provide reasonable area SM during monsoon seasons.
Dente et al. (2012b)	Maqu network, period of 2010	Soil Moisture and Ocean Salinity (SMOS) Level 2 SM product	The SMOS product exhibits a systematic dry bias ( $0.13 \text{ m}^3 \text{ m}^{-3}$ ) at the Maqu network.
Zeng et al. (2015)	Maqu network, period between 2008 and 2010	SMOS Level 3 SM product (version 2.45), Advanced Microwave Scanning Radiometer for Earth Observation System SM products (AMSR-E) SM products developed by National Aeronautics and Space Administration (NASA version 6), Land Parameter Retrieval Model (LPRM version 2), and Japan Aerospace Exploration Agency (JAXA version 700), AMSR2 Level 3 SM product (version 1.11), Advanced Scatterometer SM product (ASCAT version TU-Wien-WARP 5.5), ERA-Interim SM product (version 2.0), and Essential Climate Variable SM product (ECV version 02.0)	i) The ECV and ERA products give the best performance, and all products are able to capture the SM dynamic except for the NASA product. ii) The JAXA AMSR-E/AMSR2 products underestimate SM, while the ASCAT product overestimates it. iii) The SMOS product exhibits big noise and bias, and the LPRM AMSR-E product shows a significantly larger seasonal amplitude.
Zheng et al. (2015a)	Maqu network, period between 2009 and 2010	Noah LSM (land surface model) simulations	The modified hydraulic parameterization is able to resolve the SM underestimation in the upper soil layer under wet conditions, and it also leads to better capture for SM profile dynamics combined with the modified root distribution.
Bi & Ma (2015)	Maqu network, period between 2008 and 2011	GLDAS SM products produced by Noah, Mosaic CLM and Variable Infiltration Capacity (VIC) models	The SM simulated by the four LSMs can give reasonable SM dynamics but still show negative biases probably resulted from the high soil organic carbon content.
Li et al. (2018)	Maqu network, period between 2015 and 2016	Soil Moisture Active Passive (SMAP) Level 3 standard (36km) and enhanced (9km) passive SM products (version 3), Community Land Model (CLM4.5) simulations	i) The standard and enhanced SMAP products have similar performance for SM spatial distributions. ii) The SM of enhanced SMAP product exhibits good agreement with the CLM4.5 SM simulation.
Zhao et al. (2017)	Maqu network, period between 2008 and 2010	Downscaled SM from five typical triangle-based empirical SM relationship models	The model treating the surface SM as a second-order polynomial with LST, vegetation indices, and surface albedo outperforms other models.
Ju et al. (2019)	Maqu network, period of 2012	VIC LSM simulations	The IEPFM (immune evolution particle filter with Markov chain Monte Carlo simulation) is able to mitigate particle impoverishment and provide better assimilation results.
Zheng et al. (2018b)	Ngari network, period between 2015 and 2016	SMAP Level 2 radiometer SM product	Modifying surface roughness and employing soil temperature and texture information can improve the SMAP SM retrievals for the desert ecosystem of the TP.
Zhang et al. (2018)	Maqu and Ngari networks, period between 2010 and 2013	ERA-Interim SM product, MERRA SM product, GLDAS_Noah SM product (version2.0 and version2.1)	All these products exhibit overestimation at the Ngari network while underestimation at the Maqu network except for the ERA-Interim product.



Zheng et al. (2018a)	Maqu and Ngari networks, period between 2015 and 2016	SMAP Level 1C radiometer brightness temperature products (version 3)	<ul style="list-style-type: none"> <li>i) The SMAP algorithm underestimates the significance of surface roughness while overestimates the impact of vegetation.</li> <li>ii) The modified brightness temperature simulation can result in better SM retrievals.</li> </ul>
Wei et al. (2019)	Maqu and Ngari networks, period between 2015 and 2016	SMAP Level 3 SM passive product	The downscaled SM still can keep accuracy compared to the SM of original SMAP product.
Liu et al. (2019)	Maqu and Ngari networks, period between 2012 and 2016	SMAP Level 3 SM products (version 4.00), SMOS-IC SM products (version 105), Fengyun-3B Microwave Radiation Image SM product (FY3B MWRI), JAXA AMSR2 Level 3 SM product, LPRM AMSR2 Level 3 SM product (version 3.00)	<ul style="list-style-type: none"> <li>i) The JAXA AMSR2 product underestimates area SM while the LPRM AMSR2 product overestimates it.</li> <li>ii) The SMOS-IC product exhibits some noise of SM temporal variation.</li> <li>iii) The SMAP product has the highest accuracy among the five products while FY3B shows relatively lower accuracy.</li> </ul>
Yang et al. (2020)	Maqu and Ngari network, period between 2008 and 2011	AMSR-E brightness temperature product	The assimilated SM products exhibit higher accuracy than the AMSR-E product and LSM simulations for wet areas, whereas their accuracy is similar for dry areas.
Su et al. (2013)	Maqu and Naqu networks, period between 2008 and 2009.	AMSR-E SM product, ASCAT Level 2 SM product, ECMWF SM analyses i.e. optimum interpolation and extended Kalman filter products	<ul style="list-style-type: none"> <li>i) The Naqu area SM is overestimated by the ECMWF products in monsoon seasons, while the Maqu area SM produced by the ECMWF is comparable to previous studies.</li> <li>ii) The SM estimate cannot be considerably improved by assimilating ASCAT data due to the CDF matching approach and the data quality.</li> </ul>
Zeng et al. (2016)	Maqu, Naqu and Ngari networks, period between 2010 and 2011	LPRM AMSR-E SM product, ERA-Interim SM product	The blended SM is able to capture temporal variations across different climatic zones over the TP.
Cheng et al. (2019)	Maqu, Naqu and Ngari networks, period of 2010	European Space Agency Climate Change Initiative Soil Moisture SM product (ESA CCISM version 4.4), ERA5 SM product	<ul style="list-style-type: none"> <li>i) The seasonal variation and spatial distribution of SM can be captured by all four products i.e., ESA CCI_active, ESA CCI_passive, ESA CCI_combined, and ERA5.</li> <li>ii) The ESA CCI_active and ESA CCI_combined products exhibit narrower magnitude than the ESA CCI_passive and ERA5 products.</li> <li>iii) The SM uptrend across the TP can be found from the ERA5 product.</li> </ul>

**Table 2. Data records of all the SMST monitoring sites performed for the Maqu network. Blank cells represent that there are no measurements performed. Cells with hyphen represent that data is available. The number in cells represents the month(s) when the data is missing during a year.**

	2009	2010	2011	2012	2013	2014	2015	2016	2017	2018	2019	Data length (months)
CST01	—	—	10~12	1~6 10~12								36
CST02	—	—	5~12	1~10	6	7~12						46
CST03	—	—	—	—	6~12	1~10	7~12			1~9	5~12	68
CST04	1~5	—	12	1~3 11~12	1~2 6	8~10	7~12		1~6	7~12		73
CST05	—	—	—	—	6	—	—	5~7	—	1~2	6~12	119
NST01	1~5	—	—	—	6	—	—	5~7	—	—	6~12	116
NST02	1~3	—	—	7~8 10~12								40
NST03	—	—	5~10	—	6	—	—	5~7	—	—	6~12	115
NST04	—	—	10~12									33
NST05	3~5	—	—	—	6~12	1~7	—	5~7	7~12	1~7	6~12	92
NST06	—	1~3 12	1~3	—	6	—	—	6~7	8~12	1~7	6~12	104
NST07	—	—	3	—	6, 12	1	12	1~2 7,12	1~2 12	1~3 9~12		101
NST08	—	2, 4 9~12	1~5	—	6~10	1~10	—	6~7	—	—	6~12	95
NST09	1, 12	1~4 12	1~3	—	1~2 6	7~10	12	1~3 7, 12	1~2 7	—	6~12	99
NST10	—	11~12	1~5 7~12	1~6	6~12					1~7	6~12	44
NST11	—	—	—	7~8	6	7~12						63
NST12	10~12	1~9	—	—	6~12	1~10	7~12					49
NST13	—	—	—	—	6	—	7~12					77
NST14	6~9	—	—	—	6	10~12						64
NST15	—	10~12	1~5	6~12								33
NST21						1~7	7~12					11
NST22						1~7	7~12					11
NST24						1~7	2~12	1~7	—	—	6~12	40
NST25						1~7	—	2~12	1~8	—	6~12	39
NST31									1~8	7~12		10
NST32										1~5	6~12	12

Table 3. Same as the Table 2 but for the Ngari network.

	2010	2011	2012	2013	2014	2015	2016	2017	2018	2019	Data length (months)
<b>Shiquanhe network</b>											
SQ01	1-7	—	—	—	9-12	1-9					52
SQ02	1-7	—	—	—	5-9	—	—	—	—	9-12	104
SQ03	1-7	—	—	—	8-9	—	—	—	—	9-12	107
SQ04	1-7	—	9-12								25
SQ05	1-7	—	—	—	5-12						45
SQ06	1-7	—	9-12	1	2-9	—	—	—	—	9-12	96
SQ07	1-7	—	—	9-12	1-8	—	7-8	7-8	—	9-12	93
SQ08	1-7	8-12		1-8	8-9	—	—	—	—	9-12	82
SQ09	1-7	—	9-12	1-8	9-12						37
SQ10		1-8	—	—	7-12	1-9	7-12	1-8	—	9-12	67
SQ11	1-7	—	—	9-12					1-8	9-12	49
SQ12	1-7	—	9-12								25
SQ13	1-7	8-12									12
SQ14	1-7	—	—	—	6 8-9	—	—	—	—	9-12	106
SQ16	1-7	7-8	—	—	3-8	9-12					53
SQ17							1-8	—	—	9-12	36
SQ18							1-8	1	9-12		23
SQ19							1-8	—	—	9-12	36
SQ20							1-8	—	—	9-12	36
SQ21							1-8	—	—	9-12	36
<b>Ali network</b>											
Ail	1-7	—	9-12	1-8				1-8	8-12		40
Ali01	1-7	8-12	1-8	—	8	—	—	—	8-12		82
Ali02	1-7 11-12	1-8	—	—	8	—	—	—	8-12		85
Ali03	1-7	—	—	3-12	1-8	—	—	—	8-12		78

Table 4. Same as the Table 2 but for the Naqu network.

	2010	2011	2012	2013	2014	2015	2016	2017	2018	2019	Data length (months)
Naqu	1-7	—	—	8-9	6-8	6-9	—	9-12	1-8	9-12	88

East		1~8	—	9~12							24
West	1~7	1~8	—	1~9	7~12	1~7	8~12				42
North		1~8 11~12	1~3 9	9~12			1~8	9~12	1~8	9~12	42
South		1~8	9~12								12
Kema				1~9	3~9	—	8~12				26
MS	1~7	—	10~12	1~9	8~9 11~12	1~5	—	9~12	1~8	9~12	76
NQ01									1~8	9~12	12
NQ02									1~8	9~12	12
NQ03							1~8	9~12	1~8	9~12	24
NQ04									1~8	9~12	12

715

**Table 5. Error statistics computed between the  $SM_{AA-min}$  and the three model-based SM products for the Maqu and Shiquanhe networks.**

	Bias ( $m^3 m^{-3}$ )	RMSE ( $m^3 m^{-3}$ )	Bias ( $m^3 m^{-3}$ )	RMSE ( $m^3 m^{-3}$ )
	Warm season		Cold season	
Maqu				
ERA5-land	0.050	0.067	-	-
GLDAS Noah	-0.112	0.125	-0.049	0.088
MERRA2	-0.113	0.124	0.006	0.097
Shiquanhe				
ERA5-land	0.002	0.079	-	-
GLDAS Noah	0.010	0.116	0.052	0.058
MERRA2	0.054	0.069	0.049	0.053

**Table 6. Percentages of the site combinations that fall into an accuracy requirement in terms of RMSE.**

RMSE	0.004	0.006	0.008	0.010	0.012	0.014	0.016	0.018	0.020
Maqu network									
n=1 (%)									
n=2 (%)								0.74	3.68
n=3 (%)						0.44	1.32	3.97	7.79
n=4 (%)					0.21	1.05	3.74	9.16	16.93
n=5 (%)				0.03	0.58	3.10	9.31	18.23	28.18
n=6 (%)				0.09	1.87	8.27	19.18	31.22	42.36
n=7 (%)				0.69	6.21	18.11	31.91	43.98	54.32
n=8 (%)			0.08	3.29	14.97	30.32	43.97	55.36	64.79
n=9 (%)			0.84	9.58	26.27	42.42	55.47	65.94	74.16
n=10 (%)		0.01	3.91	19.74	38.94	54.41	66.13	75.21	82.23

n=11 (%)		0.53	11.10	32.92	51.7	65.66	75.9	83.32	88.87
n=12 (%)		3.52	23.95	47.3	64.03	75.87	84.45	90.14	94.30
n=13 (%)	0.29	13.82	39.87	61.81	75.67	85.38	91.55	95.38	97.77
n=14 (%)	3.68	32.35	57.79	74.85	86.47	92.79	96.91	98.82	99.41
n=15 (%)	21.32	56.62	75.00	88.97	95.59	98.53	99.26	100.00	100.00
n=16 (%)	52.94	82.35	94.12	94.12	100.00	100.00	100.00	100.00	100.00
Shiquanhe network									
n=1 (%)							8.33	16.67	25.00
n=2 (%)		1.52	1.52	4.55	13.64	30.30	37.88	42.42	48.48
n=3 (%)		6.82	21.36	25.45	33.18	42.73	53.18	59.55	65.00
n=4 (%)	1.62	11.31	29.7	41.41	51.11	57.37	63.23	70.51	77.58
n=5 (%)	3.66	23.11	36.87	49.12	60.23	68.18	76.14	82.32	88.26
n=6 (%)	11.36	30.95	44.37	59.85	70.24	79.11	85.28	90.15	93.29
n=7 (%)	20.20	39.77	56.06	68.31	77.90	86.87	93.43	96.84	98.48
n=8 (%)	29.29	50.51	62.63	77.58	89.09	96.57	97.98	98.99	99.60
n=9 (%)	33.64	59.55	82.73	91.36	96.36	98.18	99.55	99.55	100.00
n=10 (%)	48.48	78.79	92.42	96.97	96.97	100.00	100.00	100.00	100.00
n=11 (%)	83.33	91.67	100.00	100.00	100.00	100.00	100.00	100.00	100.00

720

**Table 7. The combinations of monitoring sites ranked by RMSE values of average SM at the Maqu network.**

Rank	Site1	Site2	Site3	Site4	Site5	Site6	Site7	Site8	Site9	Site10	Site11	Site12	RMSE
1	CST01	CST02	NST02	NST03	NST04	NST05	NST06	NST07	NST10	NST13	NST14	NST15	0.00402
2	CST01	CST02	CST04	NST01	NST02	NST03	NST04	NST05	NST06	NST07	NST13	NST15	0.00417
3	CST02	NST01	NST02	NST03	NST04	NST05	NST06	NST07	NST10	NST13	NST14	NST15	0.00450
4	CST01	CST02	NST01	NST02	NST03	NST04	NST05	NST06	NST07	NST13	NST14	NST15	0.00450
5	CST01	CST02	CST03	NST02	NST03	NST04	NST05	NST06	NST07	NST10	NST14	NST15	0.00451
96	CST01	CST02	CST03	CST04	CST05	NST03	NST06	NST10	NST11	NST13	NST14	NST15	0.00555
97	CST01	CST02	CST03	NST01	NST02	NST04	NST05	NST06	NST11	NST13	NST14	NST15	0.00555
98	CST01	CST02	CST03	CST04	CST05	NST01	NST02	NST05	NST06	NST10	NST11	NST15	0.00556
99	CST03	NST02	NST03	NST04	NST05	NST06	NST07	NST10	NST11	NST13	NST14	NST15	0.00557
<b>100</b>	<b>CST02</b>	<b>CST03</b>	<b>CST05</b>	<b>NST01</b>	<b>NST03</b>	<b>NST05</b>	<b>NST06</b>	<b>NST10</b>	<b>NST11</b>	<b>NST13</b>	<b>NST14</b>	<b>NST15</b>	<b>0.00557</b>

**Appendix A. Basic information of the Tibet-Obs**

725 **Table A1. Site information of the Maqu network (site name, elevation, topography (TPG), land cover (LC), soil texture at 5-15 cm depth (STX), soil bulk density at 5cm depth (BD), soil organic matter content at 5-15cm depth (OMC), Not Available (NA), BD and OMC values are measured in the laboratory).**

Site name	Elevation (m)	TPG	LC	STX	BD (kg m <sup>-3</sup> )	OMC (g/kg)
CST01	3431	River valley	Grass	NA	NA	NA
CST02	3449	River valley	Grass	NA	NA	NA
CST03	3507	Hill valley	Grass	NA	NA	NA
CST04	3504	Hill valley	Grass	NA	NA	NA
CST05	3542	Hill valley	Grass	NA	NA	NA
NST01	3431	River valley	Grass	Silt loam	0.96	18
NST02	3434	River valley	Grass	Silt loam	0.81	18
NST03	3513	Hill slope	Grass	Silt loam	0.63	49
NST04	3448	River valley	Wetland	Silt loam	0.26	229
NST05	3476	Hill slope	Grass	Silt loam	0.75	22
NST06	3428	River valley	Grass	Silt loam	0.81	23
NST07	3430	River valley	Grass	Silt loam	0.58	23
NST08	3473	Valley	Grass	Silt loam	1.06	34
NST09	3434	River valley	Grass	Sandy loam	0.91	17
NST10	3512	Hill slope	Grass	Loam-silt loam	1.05	24
NST11	3442	River valley	Wetland	Organic soil	0.24	136
NST12	3441	River valley	Grass	Silt loam	1.02	39
NST13	3519	Valley	Grass	Silt loam	0.67	29
NST14	3432	River valley	Grass	Silt loam	0.68	30
NST15	3752	Hill slope	Grass	Silt loam	0.78	56
NST21	3428	River valley	Grass	Silt loam	NA	NA
NST22	3440	River valley	Grass	Silt loam	NA	NA
NST24	3446	River valley	Grass	Silt loam	NA	NA
NST25	3600	Hill slope	Grass	Silt loam	NA	NA
NST31	3490	NA	NA	NA	NA	NA
NST32	3490	Hill valley	Grass	NA	NA	NA

730 **Table A2. Soil moisture with temporal persistence for the Maqu network. Cells with hyphen represent that no data is missing, cells with “M” indicate data is missing with little influence.**

Time	2009.11~ 2010.11	2010.11.~ 2011.11	2011.11~ 2012.11	2012.11~ 2013.11	2013.11~ 2014.11	2014.11~ 2015.11	2015.11~ 2016.11	2016.11~ 2017.11	2017.11~ 2018.11
CST05	—	—	—	—	—	—	—	—	—
NST01	—	—	—	—	—	—	M	—	—
NST03	—	M	—	—	—	—	M	—	—
NST06	—	M	—	—	—	—	—		
NST07	—	—	—	—	—	—			
NST13	—	—	—	—	—	—			
NST01	—	—	—	—					
NST14	—	—	—	—					
CST03	—	—	—						
NST05	—	—	—						
CST01	—	—							
CST04	—	—							
NST02	—	—							
NST04	—	—							
CST02	—								
NST10	—								
NST15	—								

**Table A3. Same as the Table A1 but for the Ngari network (BD and OMC data are not available).**

Site name	Elevation (m)	TPG	LC	STX
Shiquanhe network				
SQ01	4306	Flat	Desert	Loamy sand
SQ02	4304	Gentle slope	Desert	Sand
SQ03	4278	Gentle slope	Desert (with sparse bushes)	Sand
SQ04	4269	Edge of a wetland	Sparse grass	Loamy sand
SQ05	4261	Edge of a marsh	Sparse grass	Sand
SQ06	4257	Flat	Sparse grass	Loamy Sand
SQ07	4280	Flat	Desert (with sparse bushes)	Sand
SQ08	4306	Flat	Desert	Sand
SQ09	4275	Flat	Desert/river bed	Sand
SQ10	4275	Flat	Grassland	Fine sand with some thick roots
SQ11	4274	Flat	Grassland with bushes	Loamy sand
SQ12	4264	Flat	Edge of riverbed	Sandy loam
SQ13	4292	Flat	Valley bottom	Sand

SQ14	4368	Slope	Desert	Sandy loam
SQ16	4288	Flat	Desert/river bed	Loam
SQ17	4563	NA	NA	NA
SQ18	4634	NA	NA	NA
SQ19	4647	NA	NA	NA
SQ20	4695	NA	NA	NA
SQ21	4606	NA	NA	NA
Ali network				
Ali	4288	Flat	Grass	Loamy sand
Ali01	4262	Flat	Sparse grass	Sand
Ali02	4266	Flat	Sparse grass	Sand
Ali03	4261	Edge of a wetland	Grass	Sand

**Table A4. Same as Table A2 but for the Shiquanhe network.**

Time	2010.8~ 2011.8	2011.8~ 2012.8	2012.8~ 2013.8	2013.8~ 2014.8	2014.8~ 2015.8	2015.8~ 2016.8	2016.8~ 2017.8	2017.8~ 2018.8	2018.8~ 2019.8
SQ02	—	—	—	M	—	—	—	—	—
SQ03	—	—	—	—	—	—	—	—	—
SQ06	—	—	M	M	—	—	—	—	—
SQ14	—	—	—	—	—	—	—	—	—
SQ08				—	—	—	—	—	—
SQ07					—	—	—	—	—
SQ17							—	—	—
SQ19							—	—	—
SQ20							—	—	—
SQ21							—	—	—
SQ10								—	—
SQ11									—

735

**Table A5. Same as the Table A1 but for the Naqu network (BD and OMC data are not available).**

Site name	Elevation (m)	TPG	LC	STX
Naqu	4509	Plain	Grassland	Loamy sand
East	4527	Flat hill top	Grassland	Loamy sand
West	4506	Plain	Grassland	Loamy sand
North	4507	Slope on riverbank	Grassland	Loamy sand
South	4510	Slope of wetland	Wetland	Loamy sand



Kema	4465	River valley	Grass	Silt loam
MS	4583	NA	NA	NA
NQ01	4517	NA	NA	NA
NQ02	4552	NA	NA	NA
NQ03	4638	NA	NA	NA
NQ04	4632	NA	NA	NA

## Appendix B. Spatial upscaling methods

### B.1 Arithmetic averaging

The arithmetic averaging method assigns an equal weight coefficient to each SM monitoring site of the network, which can be formulated as:

$$\bar{\theta}_t^{ups} = \frac{1}{N} \sum_{i=1}^N \theta_{t,i}^{obs} \quad (B1)$$

where  $i$  represents the  $i^{\text{th}}$  SM monitoring site.

### B.2 Voronoi diagram

The Voronoi diagram method divides the network area into several parts according to the distances between each SM monitoring site. This approach determines the weight of each site ( $w_i$  [-]) based on the geographic distribution of all the SM monitoring sites within the network area, which can be formulated as:

$$\bar{\theta}_t^{ups} = \frac{\sum_{i=1}^N w_i \theta_{t,i}^{obs}}{\sum_{i=1}^N w_i} \quad (B2)$$

### B.3 Time stability

The time stability method is based on the assumption that the spatial SM pattern over time tends to be consistent (Vachaud et al., 1985), and the most stable site can be regarded as the representative site of the network. For each SM monitoring site  $i$  within the time window ( $M$  days in total), the mean relative difference  $MRD_i$  [-] and standard deviation of the relative difference  $\sigma(RD_i)$  [-] are estimated as:

$$\sigma(RD_i) = \sqrt{\frac{1}{M-1} \sum_{t=1}^M (RD_{t,i} - MRD_i)^2} \quad (B3)$$

$$MRD_i = \frac{1}{M} \sum_{t=1}^M \frac{\theta_{t,i}^{obs} - \bar{\theta}_t^{obs}}{\bar{\theta}_t^{obs}} \quad (B4)$$

$$RD_{t,i} = \frac{\theta_{t,i}^{obs} - \bar{\theta}_t^{obs}}{\bar{\theta}_t^{obs}} \quad (B5)$$

where  $\theta_{t,i}^{obs}$  [ $\text{m}^3 \text{m}^{-3}$ ] represents the SM measured on the  $t^{\text{th}}$  day at the  $i^{\text{th}}$  monitoring site,  $\bar{\theta}_t^{obs}$  [ $\text{m}^3 \text{m}^{-3}$ ] represents the mean SM measured at all available monitoring sites on the  $t^{\text{th}}$  day.  $MRD_i$  quantifies the bias of each SM monitoring site to identify a particular location is wetter or drier than regional mean, and  $\sigma(RD_i)$

characterizes the precision of the SM measurement. Jacobs et al., (2004) combined above two statistical  
760 metrics as a comprehensive evaluation criterion ( $CEC_i$  [-]):

$$CEC_i = \sqrt{(MRD_i)^2 + \sigma(RD_i)^2} \quad (B6)$$

The most stable site is identified by the lowest  $CEC_i$  value.

#### B.4 Apparent thermal inertia

The apparent thermal inertia (ATI) method is based on the close relationship between apparent thermal inertia  
765 ( $\tau$  [ $K^{-1}$ ]) and SM ( $\theta$  [ $m^3 m^{-3}$ ]) (Van doninck et al., 2011; Veroustraete et al., 2012). If the true areal SM ( $\bar{\theta}_t^{tru}$   
[ $m^3 m^{-3}$ ]) is available, then the weight vector  $\beta$  can be derived by the ordinary least-squares (OLS) method  
that minimizes the cost function  $J$  as:

$$J = \sum_{t=1}^M (\theta_t^{tru} - \beta^T \theta_t^{obs})^2 \quad (B7)$$

However, the  $\theta_t^{tru}$  [ $m^3 m^{-3}$ ] is usually not available in practice, and the representative SM ( $\bar{\theta}_t^{rep}$  [ $m^3 m^{-3}$ ]) is  
770 thus introduced that contains random noise but with no bias. Since the OLS method may results in overfitting  
with usage of the  $\bar{\theta}_t^{rep}$ , a regularization term is introduced and Eq. (B7) can be re-formulated as (Tarantola,  
2005):

$$J = \sum_{t=1}^M (\bar{\theta}_t^{rep} - \beta^T \theta_t^{obs})^2 \sigma^{-2} (\bar{\theta}_t^{rep} - \beta^T \theta_t^{obs}) + R \beta^T \beta \quad (B8)$$

where  $\sigma$  [ $m^3 m^{-3}$ ] represents the standard deviation of  $\bar{\theta}_t^{rep}$ ,  $R$  [-] is the regularization parameter.

775 The core issue of the ATI approach is to obtain the  $\bar{\theta}_t^{rep}$  and minimize the cost function of Eq. (B8) to obtain  
 $\beta$  and  $R$ . The  $\bar{\theta}_t^{rep}$  can be retrieved from the apparent thermal inertia  $\tau$  via empirical regression  $g(\tau)$ , and  $\tau$   
has strong connection with the surface status, e.g. land surface temperature and albedo, which is defined as:

$$\tau = C \frac{1-a}{A} \quad (B9)$$

where  $C$  [-] represents the solar correction factor,  $a$  [-] represents the surface albedo, and  $A$  [K] represents  
780 the amplitude of the diurnal temperature cycle. The albedo and land surface temperature data obtained from  
the MODIS MCD43A3 and MYD11A1/MOD11A1 Version 6 products are used to derive the ATI according  
to Eq. (B9) in this study.

The solar correlation factor  $C$  in Eq. (B9) is computed as:

$$C = \sin\varphi \sin\delta (1 - \tan^2\varphi \tan^2\delta)^{1/2} + \cos\varphi \cos\delta \arccos(-\tan\varphi \tan\delta) \quad (B10)$$

785 with

$$\delta = 0.00691 - 0.399912 \cos(\gamma) + 0.070257 \sin(\gamma) - 0.006758 \cos(2\gamma) + 0.000907 \sin(2\gamma) - \\ 0.002697 \cos(3\gamma) + 0.00148 \sin(3\gamma) \quad (B11)$$

and

$$\gamma = \frac{2\pi(n_d-1)}{365.25} \quad (B12)$$

790 where  $\varphi$  represents the latitude [rad],  $\delta$  represents the solar declination [rad], and  $n_d$  represents the Julian  
day number.

The amplitude of the diurnal LST  $A$  is estimated as  $LST_{\max} - LST_{\min}$  for a single day. Finally, we use the regression analysis between *in situ* SM measurements ( $\theta$ ) at each monitoring site and corresponding ATI ( $\tau$ ) to obtain the  $g(\cdot)$  form.

795 There are 17 and 12 monitoring sites participate in the regression analysis for the Maqu and Shiquanhe networks during the periods of 11/2009-10/2010 and 8/2018-7/2019, respectively. The ATI cannot be obtained for each monitoring site in every day since the satellite-based LST data are contaminated by clouds. In order to make full use of the data, we make the ATI-SM pair for the 1<sup>st</sup> monitoring site on the 1<sup>st</sup> day as No. 1, the pair for the 17<sup>th</sup> (or 12<sup>th</sup>) monitoring site in the Maqu (or Shiquanhe) network on the 1<sup>st</sup> day as the  
800 No. 17 (or No. 12), the pair for the 1<sup>st</sup> monitoring site at the 2<sup>nd</sup> day as the No. 18 (No. 13), and so on. Later on, we select a certain number of ATI-SM pairs (e.g. 40, 50, 60, 70, 80, 90, and 100) as a group to compute the averaged ATI and SM and construct the most reliable (i.e. with the maximum  $R^2$ ) regression relationship between them. If the ATI or SM data at one day is missing, this pair is ignored. As shown in Fig. B1, the empirical relationship is generated from 80 pairs ATI and SM averaged for the Maqu and Shiquanhe  
805 networks.

When the empirical relationship  $g(\cdot)$  is determined, the regional-average SM can be derived from grid-averaged ATI by the function  $g(\cdot)$ , which it is regarded as  $\bar{\theta}_t^{rep}$  in Eq. (B8). Finally, the optimal  $\beta$  ( $\hat{\beta}$ ) is obtained by minimizing the cost function (i.e. Eq. (B8)), and the upscaled SM can be estimated as:

$$\bar{\theta}_t^{ups} = \hat{\beta} \theta_t^{obs} \quad (B13)$$

810 The detailed description of the ATI method is referred to Qin et al. (2013).

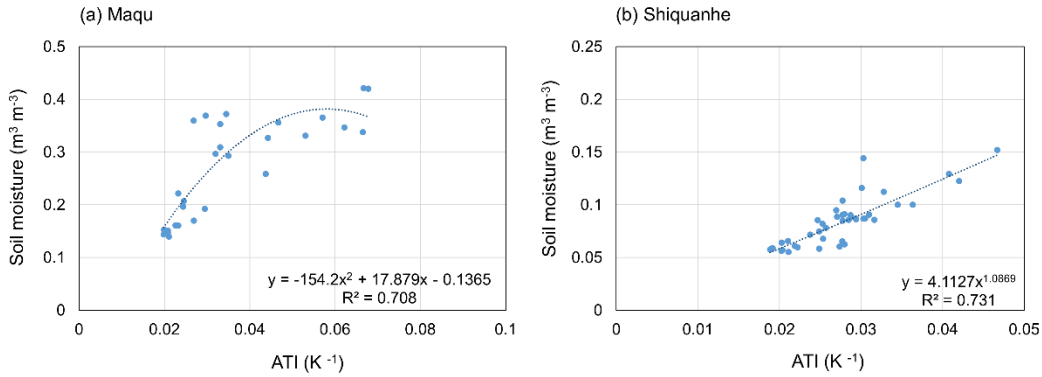
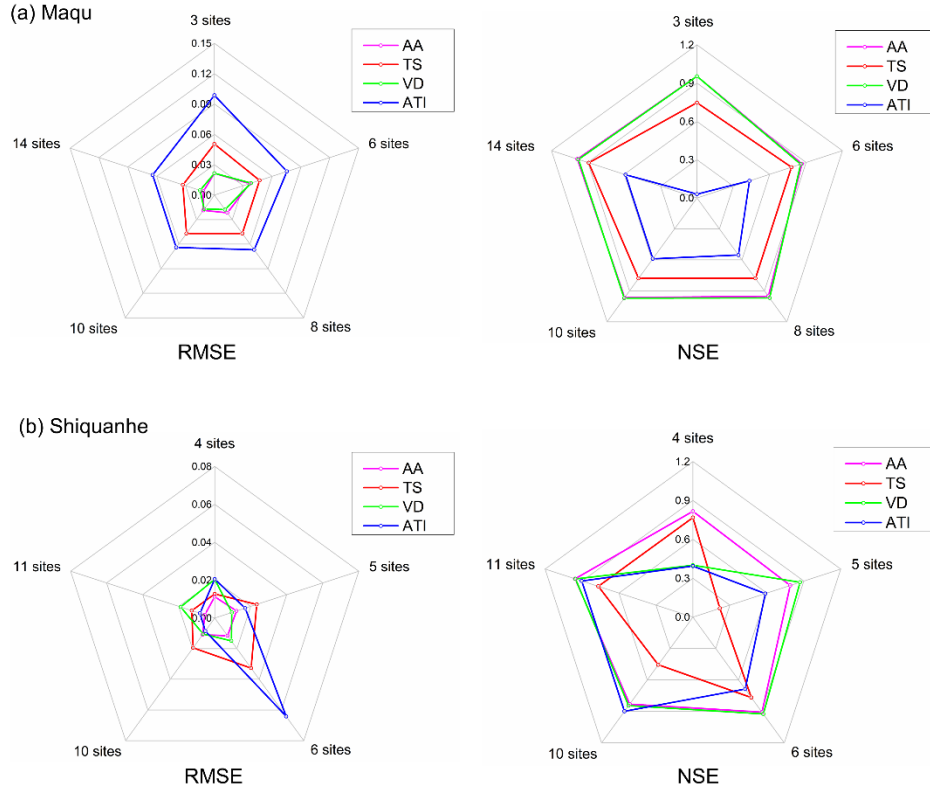


**Fig. B1 Empirical relationship between 80 pair of ATI and SM averaged for the (a) Maqu and (b) Shiquanhe networks.**



815

**Fig. B2. Radar diagram of error statistics (i.e. RMSE and NSE) computed between the  $SM_{truth}$  produced by the AA-max and the upscaled SM produced by the four upscaling methods with input of different number of available monitoring sites for the (a) Maqu and (b) Shiquanhe networks.**

820

**Table B1. Evaluation metrics computed for the upscaled SM produced with four methods with input of the maximum available monitoring sites.**

Methods	Maqu			Shiquanhe		
	MRD	$\sigma(RD)$	CEC	MRD	$\sigma(RD)$	CEC
AA-max	0.009	0.054	<b>0.055</b>	0.012	0.046	<b>0.047</b>
TS-max	0.022	0.089	0.092	0.011	0.114	0.114
VD-max	-0.026	0.064	0.069	-0.042	0.033	0.053
ATI-max	-0.005	0.145	0.145	0.016	0.068	0.070

**Table B2. Error statistics computed between the SM obtained by the four upscaling methods with input of the minimum available monitoring sites, and the  $SM_{truth}$  produced by the AA-max for the Maqu and Shiquanhe networks.**

	Bias ( $m^3 m^{-3}$ )	RMSE( $m^3 m^{-3}$ )	ubRMSE ( $m^3 m^{-3}$ )	NSE
	Maqu			
AA-min	0.005	0.022	0.021	0.954
TS-min	0.025	0.050	0.044	0.747
VD-min	-0.007	0.022	0.020	0.954
ATI-min	-0.052	0.099	0.084	0.030
Shiquanhe				

AA-min	0.010	0.011	0.005	0.816
TS-min	-0.001	0.013	0.013	0.768
VD-min	0.019	0.020	0.006	0.400
ATI-min	-0.001	0.021	0.021	0.393

---

825